Test of Cosmic Web-feeding Model for Star Formation in Galaxy Clusters in the COSMOS Field

Eunhee Ko, Myungshin Im, Seong-Kook Lee, Clotilde Laigle

To cite this version:

Eunhee Ko, Myungshin Im, Seong-Kook Lee, Clotilde Laigle. Test of Cosmic Web-feeding Model for Star Formation in Galaxy Clusters in the COSMOS Field. The Astrophysical Journal, 2024, 976, 10.3847/1538-4357/ad86c2 . insu-04851483

HAL Id: insu-04851483
https://insu.hal.science/insu-04851483v1

Submitted on 21 Dec 2024

The Astrophysical Journal, 976:154 (17pp), 2024 December 1 https://doi.org/10.3847/1538-4357/ad86c2

Test of Cosmic Web-feeding Model for Star Formation in Galaxy Clusters in the COSMOS Field

Eunhee Ko (고은희)[1,2], Myungshin Im[1], Seong-Kook Lee[1], and Clotilde Laigle[2]
[1] SNU Astronomy Research Center, Astronomy Program, Department of Physics and Astronomy, Seoul National University, Seoul 08826, Republic Of Korea; myungshin.im@gmail.com
[2] Institut d'Astrophysique de Paris, UMR 7095, CNRS, Sorbonne Université, 98 bis boulevard Arago, F-75014 Paris, France

Received 2023 December 20; revised 2024 August 27; accepted 2024 August 30; published 2024 November 20

Abstract

It is yet to be understood how large-scale environments influence star formation activity in galaxy clusters. One recently proposed mechanism is that galaxy clusters can remain star forming when fed by infalling groups and star-forming galaxies from large-scale structures (LSSs) surrounding them (the "web-feeding" model). Using the COSMOS2020 catalog that has half a million galaxies with high-accuracy ($\sigma_{\Delta z/1+z} \sim 0.01$) photometric redshifts, we study the relationship between star formation activities in galaxy clusters and their surrounding environment to test the web-feeding model. We first identify 68 cluster candidates at $0.3 \leqslant z \leqslant 1.4$ with halo masses at $10^{13.0}$–$10^{14.5}\, M_\odot$ and the surrounding LSSs with the friends-of-friends algorithm. We find that clusters with low fractions of quiescent galaxies tend to be connected with extended LSSs as expected in the web-feeding model. We also investigated the time evolution of the web-feeding trend using the `IllustrisTNG` cosmological simulation. Even though no clear correlation between the quiescent galaxy fraction of galaxy clusters and the significance of LSSs around them is found in the simulation, we verify that the quiescent galaxy fractions of infallers such as groups ($M_{200} \geqslant 10^{12}\, M_\odot$) and galaxies ($M_{200} < 10^{12}\, M_\odot$) are smaller than the quiescent fraction of cluster members and that infallers can lower the quiescent fraction of clusters. These results imply that cluster-to-cluster variations of quiescent galaxy fraction at $z \leqslant 1$ can at least partially be explained by feeding materials through cosmic webs to clusters.

Unified Astronomy Thesaurus concepts: Extragalactic astronomy (506); Galaxy clusters (584); Large-scale structure of the universe (902)

Materials only available in the online version of record: machine-readable table

1. Introduction

As the largest gravitationally bound objects in the Universe, galaxy clusters are useful tools for constraining cosmological models of the Universe. Galaxy clusters originate from the collapse of the overdensities in the initial density fluctuation field. These overdensities subsequently grew by accreting material from the large-scale structure (LSS). Thanks to their prominent scale in mass and size, galaxy clusters can offer unique laboratories to probe both the dynamical evolution of galaxies and gravitational models. Despite considerable progress in understanding galaxy clusters and their surrounding LSSs, it is not fully understood what factors play an important role in influencing star formation activity in galaxy clusters.

At low redshifts, galaxy clusters are known to have a higher fraction of red, early-type, and quiescent galaxies than in the field (e.g., H. Butcher & A. J. Oemler 1978; A. Aragon-Salamanca et al. 1993; G. De Lucia et al. 2007; J. P. Stott 2007). While the fraction of quiescent galaxies declines in both clusters and the field with redshift, the trend of high-density regions having a higher quiescent galaxy fraction than in field continues to $z \sim 1$ (e.g., I. Strateva et al. 2001; I. K. Baldry et al. 2004; J. Brinchmann et al. 2004; D. W. Hogg et al. 2004; M. Tanaka et al. 2005; D. Schiminovich et al. 2007). Moreover, at higher redshifts, galaxy clusters have a wide range of quiescent galaxy fractions, which require further explanation (e.g., A. Muzzin et al. 2012; S.-K. Lee et al. 2015; B. Darvish et al. 2016; L. Kawinwanichakij et al. 2017).

To produce quiescent galaxies, a galaxy quenching mechanism is necessary. There are several quenching mechanisms that turn star-forming galaxies (in the blue cloud) into passive galaxies (in the red sequence) (I. K. Baldry et al. 2004; E. F. Bell et al. 2004). Even though a clearer view of how quenching in galaxies takes place is still required, detailed explanations have been extensively built upon observational evidence (e.g., Y.-j. Peng et al. 2010; S. Alberts & A. Noble 2022). Mass quenching, also known as internal feedback, refers to all the internal processes linked to the galaxy mass, such as gas outflows driven by stellar winds or supernovae explosions (e.g., R. B. Larson 1974; A. Dekel & J. Silk 1986; C. Dalla Vecchia & J. Schaye 2008). Also, several studies suggest that the active galactic nuclei (AGN) feedback from the central supermassive black hole (e.g., D. J. Croton et al. 2006; A. C. Fabian 2012; J. J. Fang et al. 2013; C. Cicone et al. 2014; M. N. Bremer et al. 2018) plays an important role in the mass quenching. On the other hand, environmental quenching is the physical process that stops star formation in these galaxies that are interacting with the surrounding area at a larger scale than the host halo. Environmental quenching includes hydrodynamical processes such as ram pressure stripping (J. E. Gunn & J. R. I. Gott 1972) and starvation or strangulation (R. B. Larson et al. 1980). Gravitational interactions through mergers, tidal interactions, and harassment can also trigger drastic changes in star formation (e.g., B. Moore et al. 1996; R. Smith et al. 2010; D. Bialas et al. 2015). In the local universe, the environment and mass effects on quenching can be separable to some extent, thanks to the richness of spectroscopic and photometric information used to constrain both galaxy redshift, stellar mass, and stellar-to-halo mass ratio (e.g., I. K. Baldry et al. 2006; Y.-j. Peng et al. 2010; K. Kovač et al. 2014; M. L. Balogh et al. 2016; R. F. J. van der Burg et al. 2018); however, it is difficult to differentiate the two effects at higher redshift where data quality is poorer.

Because galaxies accrete the fuel for star formation from the cosmic web, it has naturally emerged as a potential factor to control quiescent galaxy fraction within galaxy clusters in the cosmological context. One proposed mechanism is cosmic web detachment (CWD), suggested by M. A. Aragon Calvo et al. (2019). According to CWD, once the primordial filaments are detached or ruptured from the node, star formation starts to decline. This model aims to explain how star formation is regulated across all mass ranges in a cosmological framework. The role of the cosmic web can be extended from galactic scales to larger scales. The filamentary structures replenish the galaxy cluster with star-forming galaxies, groups, and cold gas as they fall into the galaxy clusters through filaments. Previous studies have provided observational evidence that supports the enhanced star formation around the host cluster and nearby environment such as filaments (e.g., L. Bai et al. 2007; S. C. Porter & S. Raychaudhury 2007; D. Fadda et al. 2008; Y. Koyama et al. 2008; L. Bai et al. 2009; L. M. Lubin et al. 2009; M. Tanaka et al. 2009; S. M. Chung et al. 2010; J. E. Geach et al. 2011; B. C. Lemaux et al. 2012; S. Mahajan et al. 2012; B. Darvish et al. 2014; C.-L. Hung et al. 2016; D. Kleiner et al. 2017; I. Pintos-Castro et al. 2019; M. Einasto et al. 2020). However, there are theoretical (e.g., M. Musso et al. 2018; K. Kraljic et al. 2020) and observational (e.g., M. Alpaslan et al. 2016; M. Crone Odekon et al. 2018; C. Laigle et al. 2018; K. Kraljic et al. 2019; N. Winkel et al. 2021) works at odds with the trend. For example, H. Song et al. (2021) point out that the quenching of galaxies specifically occurs at the edge of filaments. The coherent flow from vorticity-rich filaments (e.g., C. Laigle et al. 2015; S. Lu et al. 2022) impedes the gas transfer to the inner halo and lowers the efficiency of star formation. Therefore, the exact role of the cosmic web in regulating galaxy star formation still remains elusive. One important aspect is to conduct a meticulous comparison of various studies within a consistent mass and redshift range, as the trend can vary significantly depending on the measured parameters and the scale under consideration.

Recently, Lee et al. (2019, hereafter L19) suggested the web-feeding model that elucidates the variety levels of star formation activity within clusters. By analyzing galaxies at $z \sim 1$ in the Ultra Deep Survey (UDS) field (O. Almaini et al. 2007), L19 found that member galaxies embedded within more extended structures tend to have a lower fraction of quiescent galaxies in comparison to those in isolated environments at a similar redshift. The correlation between quenched fraction and the size of connected large scale led L19 to propose that the enhanced star-forming activities in some of the overdensities at $z \sim 1$ are due to the inflow of gas and star-forming galaxies to the overdense areas from the surrounding large-scale environments.[3]

The main caveat of in L19 is that the identified structures such as galaxy clusters and surrounding filaments are susceptible to line-of-sight contamination due to large photometric redshift uncertainties of about $0.028(1+z)$. This could lead to erroneous associations of galaxy clusters with the LSS and systematic errors in the quiescent fraction of galaxies due to the misidentification of cluster members. Additionally, the result could be susceptible to cosmic variance (B. P. Moster et al. 2011). Therefore, examining the web-feeding model using an independent field with improved photometric redshift accuracy is highly desired.

In this paper, we will test the web-feeding model with the COSMOS2020 data (J. R. Weaver et al. 2022). As described in the next section, the newly released COSMOS2020 data provides photometric redshifts that are several times more accurate than those used in L19 and also contain tens of thousands of spectroscopic redshifts. Furthermore, the COSMOS field (N. Scoville et al. 2007) is nearly twice as large as the field of view of the UDS field. Thus, with the COSMOS2020 data, it is possible to significantly improve the analysis of L19. Moreover, we will also investigate the time evolution of large-scale cosmic web feeding and the respective effects of infalling structures using the `IllustrisTNG 300-1` (`TNG300`) simulation (D. Nelson et al. 2018; V. Springel et al. 2018). Throughout this work, we adopt the standard ΛCDM cosmology $(\Omega_m, \Omega_\lambda) = (0.3, 0.7)$ and $H_0 = 70\ \mathrm{km\ s^{-1}\ Mpc^{-1}}$ and AB magnitude system (J. B. Oke 1974).

2. Data

The Cosmic Evolution Survey (COSMOS) is a deep multiwavelength survey of $2\ \mathrm{deg}^2$ of the sky centered at an R.A. of 10:00:28.8 and decl. of +02:12:21.0 (N. Scoville et al. 2007). It boasts data from the X-ray to the radio, including the Hubble Space Telescope and Chandra X-ray images for studying distant galaxies at high spatial resolution. COSMOS also includes a multitude of ground-based imaging and spectroscopic data. In particular, it contains narrow- and medium-band images covering the optical to near-infrared, including NB711, NB816, and 12 medium bands from Subaru Suprime-Cam (Y. Taniguchi et al. 2007, 2015) and NB118 from the UltraVISTA survey (H. J. McCracken et al. 2015; A. Moneti et al. 2023). Moreover, ultra-deep images such as J^{UD}, H^{UD}, and K^{UD} reach 3σ depths in $3''$ diameter apertures of 25.9, 25.5, and 25.2 mag, respectively, which are useful for accurately determining photometric redshifts (see J. R. Weaver et al. 2022 for more details). More importantly, about 20,000 targets of spectroscopic redshifts have been obtained in this field largely from the zCOSMOS survey (S. J. Lilly et al. 2007) and VIMOS UDS (O. Le Fèvre et al. 2015), making it possible to test photometric redshifts thoroughly.

In this study, we use the most up-to-date publicly released catalog produced by the COSMOS2020 team (J. R. Weaver et al. 2022). Since the last public catalog in 2015 (C. Laigle et al. 2016), new photometric and spectroscopic data has been added including ultra-deep optical data from the Hyper Suprime-Cam (HSC) Subaru Strategic Program (SSP) PDR2 (H. Aihara et al. 2019), Visible Infrared Survey Telescope for Astronomy (VISTA) DR4, and Spitzer IRAC data (M. L. N. Ashby et al. 2018). With these additions, the number of detected sources doubled, and homogeneity in photometry and astrometry was improved significantly. As a result, J. R. Weaver et al. (2022) suggest that COSMOS2020

---

[3] Here, we confine the LSSs to several Mpc probing the intercluster cosmic web.

contains the most reliable photometric redshifts of galaxies in the COSMOS field at present. The photometric redshift accuracy is only subpercent for bright sources ($i < 21$) and 5% at $25 < i < 27$.

There are two versions of the COSMOS2020 catalog provided: `CLASSIC` and `The Farmer`. The source detection in the `CLASSIC` catalog is performed using `SExtractor` (E. Bertin & S. Arnouts 1996). On the other hand, `The Farmer` catalog utilizes `Tractor` (D. Lang et al. 2016), which has been developed to perform profile-fitting photometry. This model-based code enables photometry of the detected sources free from blending with close objects and from point spread function homogenization while suffering from different resolution regimes and failure of convergence for either extremely bright or dense sources. The catalogs obtained from two different photometric extraction codes are in good agreement overall, but the choice of the catalog should depend on the study's specific objectives.

For photometric redshift and spectral energy distribution (SED) fitting, the results from two separate codes are also available: `LePHARE` (S. Arnouts et al. 2002; O. Ilbert et al. 2006) and `EAZY` (G. B. Brammer et al. 2008). Compared with spectroscopic redshifts in the COSMOS field, the normalized median absolute deviation (NMAD; D. C. Hoaglin et al. 1983) of photometric redshift is of the order of $0.01(1 + z)$ at $i < 22.5$ and better than $0.25(1 + z)$ at fainter magnitudes for both cases. Even though the precision of photometric redshifts is similar between both cases, `The Farmer` has its advantages at fainter magnitudes (lower NMAD), while `CLASSIC` presents better validity at brighter sources (see Figure 13 and 15 in J. R. Weaver et al. 2022). Given our primary precondition for this study is to identify reliable galaxy cluster candidates and surrounding LSSs at relatively high redshift, we adopt a combination of The `Farmer` and `LePHARE`, which shows the smaller fraction of catastrophic failure η, the ratio of deviant galaxies from their spectroscopic redshift by $\Delta z > 0.15(1 + z_{\text{spec}})$ with similar precision.

2.1. Photometric Redshift Uncertainties

Because our goal is to find reliable cluster members and minimize the contamination from line-of-sight interlopers, we need to confine the photometric redshift uncertainty to an appropriate level. The threshold for photometric redshift uncertainty should not be too strict to avoid excluding the high-redshift region but also not too loose to avoid contaminating the cluster members in the foreground or background direction. Previous studies (M. C. Cooper et al. 2005; N. Malavasi et al. 2016; B. Darvish et al. 2017) have verified that photometric redshifts with uncertainties of $\sigma_{\Delta z/1+z} \sim 0.01$ can reliably build the density field. In the following analysis, we adopt the $0.01(1 + z)$ as a fiducial value to determine limiting quantities such as maximum redshift and limiting stellar mass.

To examine the COSMOS2020 photometric redshift accuracy, we compared the photometric redshifts from COSMOS2020 and matched spectroscopic redshifts of 8562 galaxies from zCOSMOS (S. J. Lilly et al. 2007). As shown in Figure 1, we find that the NMAD $\sigma_{\Delta z/1+z}$ is of the order of 0.01 up to a redshift of $z < 1.4$. This result is consistent with the result in J. R. Weaver et al. (2022) where they found the same order of NMAD at $17 < i < 24$ (see Figure 17 of their paper for more details). This NMAD $\sigma_{\Delta z/1+z}$ corresponds to the galaxies matched with the COSMOS2020 data, mostly brighter than the limiting magnitudes from various surveys of COSMOS2020.

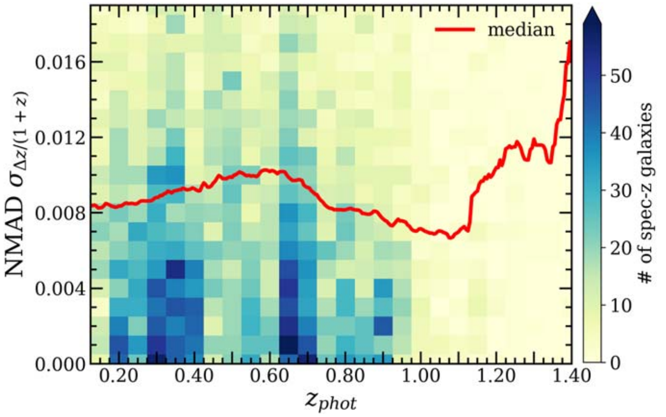

Figure 1. Photometric redshift uncertainty (NMAD, $\sigma_{\Delta z/1+z}$) as a function of photometric redshift (red line). The uncertainty is calculated by comparing photometric redshift derived from `LePHARE` with the publicly available spectroscopic redshift catalog (S. J. Lilly et al. 2007). The background 2D histogram shows the population of galaxies within the photometric redshift and uncertainty bins.

Note that this photometric redshift is applicable to the brighter galaxies with spectroscopic redshifts available. For example, the spectroscopic redshift sample has a mean and standard deviation in HSC i-band magnitudes of 21.4 and 0.9 mag, respectively, while the photometric redshift sample, used throughout the paper, has 23.7 and 1.5 mag. Although our sample includes faint galaxies, the majority ($\gtrsim$80%) of the sample is brighter than 24.9 mag at which the NMAD values are of the order of 0.02–0.03 (J. R. Weaver et al. 2022). Such an order of uncertainties, $3 \times 0.01(1 + z)$ is taken into account when finding clusters in Section 2.3.

2.2. Mass Complete Sample

To avoid the bias arising by missing faint low-mass galaxies, we construct the mass complete sample by following the empirical procedure adopted by L. Pozzetti et al. (2010) and O. Ilbert et al. (2013). The idea of this approach is to transform the detection limit of a survey, represented as the apparent magnitude m_{lim}, into the observable stellar mass limit $M_{*,\text{lim}}$ as a function of redshift. We use m_{lim} of IRAC channel 1 from the CANDELS-COSMOS catalog (H. Nayyeri et al. 2017). The m_{lim} in IRAC channel 1 is set to 26 mag, corresponding to a 3σ depth of 26.4/25.7 mag in an aperture of $2''/3''$ (I. Davidzon et al. 2017; J. R. Weaver et al. 2022). Then, we convert the apparent magnitude m_i of the ith galaxy into the stellar mass, which is scaled by an empirical mass-to-light ratio $10^{-0.4(m_i - m_{\text{lim}})}$. In the next step, we determine the 95th percentile stellar mass completeness limit, which is defined as the 95th percentile of the smallest mass at the central redshift of each redshift bin with a step size of $\Delta z = 0.05$.

The stellar mass limit at $z = 1.4$, where the uncertainty of photometric redshift is as low as $0.01(1 + z)$ to reliably build density structures, is $10^{8.75}\,M_\odot$ for all types of galaxies and $10^{8.99}\,M_\odot$ for quiescent galaxies selected based on Equation (1) as shown in Figure 2. When we construct the density field and find galaxy clusters, we apply this stellar mass cut. However, it is possible that this selection is not complete for low-mass quiescent galaxies. Therefore, we adopt the mass limit of $10^{8.99}\,M_\odot$ when we calculate the quiescent galaxy fraction (see Section 3.1). Compared with J. R. Weaver et al. (2023), we confirmed that our mass completeness limit is nearly consistent

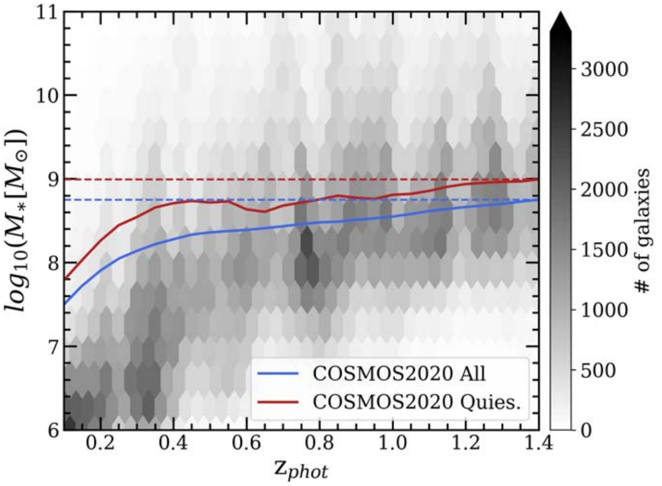

Figure 2. Mass complete limit as a function of photometric redshift. The blue solid line represents the mass complete limit of all types of galaxies while the red solid line is for quiescent galaxies only. The blue and red dashed lines indicate the mass completeness limits for all types and quiescent galaxies at $= 1.4$. We used galaxies exceeding the stellar mass limit as indicated by the blue dashed line. The background 2D histogram stands for the number of galaxies in a given redshift and stellar mass bin.

with the 70% mass completeness limit of CANDELS-COSMOS sources ($10^{8.57}\,M_\odot$ for all types of galaxies and $10^{8.91}\,M_\odot$ for quiescent galaxies).

With the information obtained from the aforementioned calculation, we select sources that are flagged as galaxies (`lp_type=0`), outside the bright source mask (`FLAG_COMBINED=0`), and more massive than the mass complete limit of $10^{8.75}\,M_\odot$. By imposing the flag condition `FLAG_COMBINED=0` obtained from combining the bright source masks in the UltraVISTA (H. J. McCracken et al. 2012), HSC-SSP (J. Coupon et al. 2018), and Suprime-Cam (Y. Taniguchi et al. 2007, 2015) regions, we can avoid the data with unreliable photometry or partial coverage. Also, we limit our study to $z \leqslant 1.4$ to construct the reliable density field using accurate $\sigma_{\Delta z/1+z} \sim 0.01$. The total number of galaxies after we applied the source flags, the stellar mass cut, and the photometric redshift cut is 110,409.

2.3. Galaxy Cluster Selection

Galaxy clusters are identified as overdense regions in the density field (E. Kang & M. Im 2015; S.-K. Lee et al. 2015). To construct the density field, we divide the galaxy sample into multiple redshift bins from $z = 0.1$ to 1.4 with a step size of $\Delta z = 0.01$. The number of galaxies in each bin nearly uniformly increases from ∼100 at $z = 0.1$ to ∼8000 at $z = 1.4$. Here, the step size is determined as the value comparable to the photometric redshift accuracy $\sigma_{\Delta z/1+z}$. For galaxy redshifts, we use photometric redshifts except when spectroscopic redshifts are available from zCOSMOS (S. J. Lilly et al. 2007). Then, in each redshift bin, we count the number of galaxies within a search radius of 700 kpc at every point that is spaced at 100 kpc. A convolution radial scale of 700 kpc is chosen to probe structures slightly smaller than a typical galaxy cluster. This value lies within the range of typical filter sizes of density maps 0.5−1.0 Mpc used to find cluster candidates (e.g., R. R. Gal et al. 2000; E. Kang & M. Im 2009; F. Sarron et al. 2018). We select galaxy cluster candidates with a surface number density exceeding four times the standard deviation from the average number density at a given redshift. Adopting the 4σ threshold, as done by L19, allows us to compare our results consistently and to identify intermediate-mass overdensities where the web-feeding trend is expected to appear. Our selection of the galaxy cluster candidates is based on the following conditions: (1) Connected 4σ level overdense grid points should be more than 10 points; (2) Overdensities should be linked along the line of sight over at least three redshift bins. The condition of the number of connected points is imposed to sample overdense regions to the approximate size of galaxy clusters corresponding to $R_{200} \sim 1$ Mpc. Furthermore, the choice of more than three redshift grids linked along the line of sight aims to detect as many candidates as possible and to avoid including the falsely overlapping structures in photometric redshifts in our sample. The completeness of this method is further investigated at the end of this section.

To determine member galaxies, the initial center coordinate (R.A., decl., z) of a cluster candidate is estimated as the number density-weighted average of the coordinates for all the connected grid points. Along the line-of-sight direction, we apply a conservative condition to protect member galaxies from contamination derived from the photometric redshift uncertainties and only select galaxies within a given redshift bin $|z| \leqslant z_{\rm grid} \pm \sigma_{\Delta z/1+z}(1+z)$, where $z_{\rm grid}$ is a redshift of a given redshift bin. Then, we calculate the transversal distance distribution of the galaxies from the initial center. The 2D distance distribution from the initial center shows a bell-like shape and we therefore fit the distribution with a Gaussian distribution. The transversal cluster boundary from the center is then determined as 3σ of the Gaussian distribution and members of a cluster candidate are defined as galaxies within the corresponding radius. As for final member candidates, we exclude galaxies whose spectroscopic redshifts (1) differ from photometric redshifts by more than 15% or (2) are outside the $\pm 3\sigma_{\Delta z/1+z}(1+z)$ range from the redshift of the cluster center. Finally, we recalculate the cluster's central position and redshift by the mass-weighted mean of member galaxies. As a result, 109 cluster candidates are identified. Furthermore, we exclude the candidates that are near the bright source masks and (or) survey edges (39/109) or that are largely elongated along the line-of-sight direction (2/109). The remaining number of candidates becomes 68. These clusters and their properties are listed in Table 1.

To verify the reliability of the identified galaxy clusters, we use the light-cone mock catalog (A. I. Merson et al. 2013) from the Millennium simulation (V. Springel 2005) and GALFORM semi-analytic model (S. Cole et al. 2000; R. G. Bower et al. 2006). To reproduce a field similar to COSMOS, we define a $1.4 \times 1.4\,\rm deg^2$ area and use galaxies more massive than the stellar mass of $10^{8.75}\,M_\odot$. Moreover, we add photometric redshift errors following the Gaussian distribution with the standard deviation σ that corresponds to the photometric redshift uncertainty at the observed redshifts. We apply the same cluster-finding method as the cluster search for the COSMOS2020 data but with a different number of the least connected redshift bins and compare the found cluster candidates to estimate the completeness of this method. There are 674 (14) halos more massive than 10^{13} $(10^{14})\,M_\odot$ at $z \leqslant 1.4$ in the reproduced field and we detected 339 halos at $10^{13}\,M_\odot \leqslant M_{200} < 10^{14}\,M_\odot$ and 14 halos at $10^{14}\,M_\odot \leqslant M_{200}$ when we adopt the same criterion in the COSMOS data. When

Table 1
Galaxy Cluster Candidates Found in the COSMOS Field

R.A. (J2000) (1)	Decl. (J2000) (2)	$z_{\rm phot}$ (3)	$\log(M_{200}/M_{\odot})$ (4)	$N_{\rm mem}$ (5)	$N_{\rm outlier}/N_{\rm spec}$ (6)	FoF Fraction (7)	QF (8)	ID (9)
150.045	2.216	$0.266^{+0.008}_{-0.007}$	$13.64^{+0.12}_{-0.06}$	23	2/12	$0.045^{+0.009}_{-0.004}$	$0.44^{+0.19}_{-0.17}$	⋯
150.306	2.016	$0.309^{+0.008}_{-0.007}$	$13.12^{+0.15}_{-0.17}$	23	1/9	$0.037^{+0.013}_{-0.009}$	$0.40^{+0.09}_{-0.10}$	20077
150.189	1.759	$0.333^{+0.009}_{-0.005}$	$13.47^{+0.11}_{-0.01}$	53	4/23	$0.016^{+0.000}_{-0.003}$	$0.68^{+0.23}_{-0.02}$	20029
149.945	2.601	$0.333^{+0.010}_{-0.006}$	$13.39^{+0.52}_{-0.27}$	29	2/15	$0.024^{+0.001}_{-0.009}$	$0.50^{+0.03}_{-0.05}$	30311
150.485	2.056	$0.431^{+0.007}_{-0.006}$	$13.50^{+0.15}_{-0.12}$	31	6/16	$0.053^{+0.017}_{-0.000}$	$0.56^{+0.03}_{-0.06}$	30315
149.964	2.207	$0.435^{+0.005}_{-0.007}$	$13.55^{+0.07}_{-0.09}$	23	5/18	$0.007^{+0.000}_{-0.000}$	$0.91^{+0.02}_{-0.08}$	20088
150.112	2.562	$0.505^{+0.008}_{-0.008}$	$13.20^{+0.07}_{-0.04}$	70	4/25	$0.024^{+0.000}_{-0.021}$	$0.43^{+0.03}_{-0.05}$	20137
150.223	1.815	$0.543^{+0.003}_{-0.009}$	$13.65^{+0.15}_{-0.00}$	83	1/35	$0.064^{+0.001}_{-0.010}$	$0.35^{+0.04}_{-0.04}$	20289
150.133	1.860	$0.547^{+0.009}_{-0.012}$	$13.89^{+0.21}_{-0.02}$	60	4/27	$0.066^{+0.013}_{-0.008}$	$0.33^{+0.13}_{-0.07}$	⋯
149.915	2.523	$0.602^{+0.008}_{-0.005}$	$13.31^{+0.07}_{-0.06}$	80	3/4	$0.025^{+0.005}_{-0.000}$	$0.57^{+0.06}_{-0.11}$	⋯
149.729	1.836	$0.597^{+0.010}_{-0.010}$	$13.37^{+0.20}_{-0.05}$	26	3/6	$0.089^{+0.032}_{-0.019}$	$0.28^{+0.05}_{-0.10}$	⋯
150.503	2.454	$0.626^{+0.009}_{-0.008}$	$13.44^{+0.26}_{-0.06}$	47	4/11	$0.080^{+0.003}_{-0.019}$	$0.32^{+0.18}_{-0.05}$	⋯
149.602	1.892	$0.655^{+0.005}_{-0.004}$	$13.57^{+0.20}_{-0.06}$	72	0/12	$0.031^{+0.018}_{-0.000}$	$0.25^{+0.13}_{-0.08}$	⋯
150.151	2.499	$0.658^{+0.005}_{-0.006}$	$13.39^{+0.24}_{-0.04}$	47	1/10	$0.033^{+0.001}_{-0.014}$	$0.29^{+0.04}_{-0.10}$	20035
149.927	2.104	$0.663^{+0.005}_{-0.005}$	$13.59^{+0.19}_{-0.07}$	57	3/18	$0.055^{+0.003}_{-0.000}$	$0.29^{+0.04}_{-0.08}$	⋯
150.058	2.611	$0.675^{+0.007}_{-0.015}$	$13.70^{+0.11}_{-0.16}$	59	2/15	$0.056^{+0.000}_{-0.030}$	$0.33^{+0.07}_{-0.03}$	10215
150.086	2.192	$0.697^{+0.008}_{-0.005}$	$13.78^{+0.22}_{-0.08}$	31	1/9	$0.010^{+0.036}_{-0.006}$	$0.43^{+0.08}_{-0.13}$	10216
150.052	2.308	$0.717^{+0.009}_{-0.010}$	$13.63^{+0.06}_{-0.03}$	38	0/13	$0.107^{+0.018}_{-0.001}$	$0.22^{+0.06}_{-0.10}$	⋯
150.039	2.649	$0.792^{+0.008}_{-0.005}$	$13.22^{+0.02}_{-0.10}$	28	1/4	$0.013^{+0.004}_{-0.000}$	$0.40^{+0.08}_{-0.07}$	⋯
150.532	2.160	$0.834^{+0.008}_{-0.007}$	$13.78^{+0.42}_{-0.01}$	170	1/30	$0.080^{+0.001}_{-0.022}$	$0.27^{+0.03}_{-0.02}$	⋯
150.688	2.418	$0.825^{+0.007}_{-0.006}$	$13.60^{+0.21}_{-0.12}$	33	0/1	$0.027^{+0.000}_{-0.014}$	$0.30^{+0.02}_{-0.02}$	⋯
149.651	2.386	$0.841^{+0.005}_{-0.008}$	$13.95^{+0.08}_{-0.04}$	111	2/8	$0.044^{+0.011}_{-0.000}$	$0.44^{+0.03}_{-0.02}$	30231
150.374	2.141	$0.840^{+0.006}_{-0.007}$	$13.76^{+0.05}_{-0.02}$	84	2/17	$0.097^{+0.024}_{-0.000}$	$0.26^{+0.04}_{-0.05}$	⋯
149.553	2.421	$0.837^{+0.005}_{-0.007}$	$13.78^{+0.07}_{-0.02}$	31	0/5	$0.053^{+0.004}_{-0.009}$	$0.44^{+0.03}_{-0.03}$	20106
150.453	2.142	$0.861^{+0.009}_{-0.015}$	$13.92^{+0.14}_{-0.06}$	64	3/10	$0.065^{+0.007}_{-0.020}$	$0.25^{+0.06}_{-0.03}$	⋯
150.553	2.197	$0.847^{+0.008}_{-0.007}$	$13.69^{+0.07}_{-0.02}$	54	0/9	$0.079^{+0.006}_{-0.012}$	$0.35^{+0.03}_{-0.06}$	⋯
149.985	2.321	$0.860^{+0.008}_{-0.008}$	$14.12^{+0.10}_{-0.02}$	40	6/10	$0.039^{+0.027}_{-0.007}$	$0.58^{+0.03}_{-0.03}$	⋯
150.220	2.287	$0.870^{+0.009}_{-0.007}$	$13.86^{+0.12}_{-0.16}$	42	1/7	$0.047^{+0.008}_{-0.000}$	$0.39^{+0.04}_{-0.09}$	20135
149.934	2.406	$0.886^{+0.004}_{-0.011}$	$13.77^{+0.34}_{-0.01}$	105	2/20	$0.023^{+0.019}_{-0.000}$	$0.48^{+0.11}_{-0.04}$	20187
150.088	2.533	$0.888^{+0.006}_{-0.008}$	$13.89^{+0.24}_{-0.02}$	111	1/17	$0.062^{+0.011}_{-0.006}$	$0.40^{+0.11}_{-0.06}$	10208
149.552	2.003	$0.884^{+0.005}_{-0.006}$	$13.64^{+0.31}_{-0.31}$	45	0/3	$0.009^{+0.007}_{-0.002}$	$0.29^{+0.09}_{-0.03}$	20143
149.925	2.642	$0.889^{+0.002}_{-0.007}$	$13.99^{+0.06}_{-0.01}$	196	3/30	$0.075^{+0.000}_{-0.007}$	$0.21^{+0.02}_{-0.02}$	⋯
149.671	2.257	$0.911^{+0.003}_{-0.005}$	$13.48^{+0.04}_{-0.01}$	47	0/6	$0.009^{+0.001}_{-0.000}$	$0.17^{+0.02}_{-0.03}$	⋯
149.976	2.341	$0.933^{+0.003}_{-0.005}$	$14.07^{+0.07}_{-0.06}$	205	4/48	$0.098^{+0.000}_{-0.000}$	$0.41^{+0.03}_{-0.04}$	30172
150.261	2.075	$0.930^{+0.007}_{-0.007}$	$13.62^{+0.15}_{-0.01}$	72	2/8	$0.076^{+0.002}_{-0.000}$	$0.21^{+0.01}_{-0.01}$	⋯
150.159	2.192	$0.928^{+0.003}_{-0.003}$	$13.68^{+0.12}_{-0.00}$	45	1/10	$0.117^{+0.000}_{-0.000}$	$0.18^{+0.02}_{-0.01}$	⋯
150.085	2.193	$0.932^{+0.005}_{-0.006}$	$13.78^{+0.04}_{-0.03}$	51	1/6	$0.114^{+0.002}_{-0.001}$	$0.26^{+0.04}_{-0.02}$	⋯
150.030	2.201	$0.940^{+0.004}_{-0.004}$	$13.92^{+0.13}_{-0.11}$	128	4/17	$0.117^{+0.007}_{-0.000}$	$0.22^{+0.03}_{-0.05}$	10281
150.036	2.302	$0.930^{+0.006}_{-0.004}$	$13.71^{+0.13}_{-0.03}$	51	1/12	$0.110^{+0.000}_{-0.003}$	$0.16^{+0.04}_{-0.00}$	⋯
149.652	2.343	$0.960^{+0.009}_{-0.006}$	$13.63^{+0.02}_{-0.13}$	109	2/8	$0.078^{+0.010}_{-0.000}$	$0.29^{+0.05}_{-0.04}$	30296
149.646	2.222	$0.960^{+0.006}_{-0.008}$	$13.54^{+0.01}_{-0.02}$	69	0/4	$0.084^{+0.008}_{-0.000}$	$0.29^{+0.05}_{-0.02}$	20161
149.494	2.012	$0.988^{+0.006}_{-0.006}$	$14.00^{+0.13}_{-0.02}$	106	0/3	$0.103^{+0.005}_{-0.000}$	$0.16^{+0.01}_{-0.05}$	⋯
149.748	2.267	$1.017^{+0.002}_{-0.004}$	$13.99^{+0.14}_{-0.01}$	211	14/35	$0.121^{+0.009}_{-0.000}$	$0.28^{+0.01}_{-0.02}$	⋯
149.972	1.672	$1.028^{+0.006}_{-0.003}$	$13.40^{+0.11}_{-0.06}$	40	1/3	$0.024^{+0.001}_{-0.000}$	$0.13^{+0.01}_{-0.02}$	⋯
150.704	2.312	$1.080^{+0.010}_{-0.009}$	$13.57^{+0.08}_{-0.08}$	111	0/4	$0.098^{+0.016}_{-0.007}$	$0.18^{+0.04}_{-0.03}$	20150
150.636	2.410	$1.102^{+0.004}_{-0.007}$	$13.31^{+0.11}_{-0.01}$	28	1/1	$0.066^{+0.000}_{-0.016}$	$0.17^{+0.01}_{-0.02}$	⋯
150.541	2.550	$1.136^{+0.007}_{-0.005}$	$13.91^{+0.03}_{-0.20}$	89	3/4	$0.059^{+0.001}_{-0.000}$	$0.26^{+0.04}_{-0.01}$	⋯
150.437	2.542	$1.128^{+0.007}_{-0.007}$	$13.43^{+0.06}_{-0.08}$	38	2/3	$0.053^{+0.000}_{-0.002}$	$0.17^{+0.02}_{-0.03}$	⋯
150.351	1.953	$1.148^{+0.005}_{-0.008}$	$13.55^{+0.09}_{-0.01}$	117	8/11	$0.035^{+0.000}_{-0.006}$	$0.10^{+0.03}_{-0.03}$	⋯
149.907	2.673	$1.141^{+0.004}_{-0.005}$	$13.37^{+0.13}_{-0.04}$	39	2/3	$0.012^{+0.002}_{-0.000}$	$0.10^{+0.02}_{-0.05}$	⋯
150.199	1.899	$1.181^{+0.007}_{-0.005}$	$13.41^{+0.18}_{-0.30}$	35	2/3	$0.083^{+0.000}_{-0.018}$	$0.22^{+0.03}_{-0.02}$	⋯
150.122	1.984	$1.187^{+0.005}_{-0.004}$	$13.58^{+0.01}_{-0.03}$	273	19/51	$0.092^{+0.017}_{-0.000}$	$0.25^{+0.06}_{-0.02}$	⋯
150.098	2.032	$1.190^{+0.002}_{-0.001}$	$13.83^{+0.04}_{-0.00}$	117	12/20	$0.090^{+0.000}_{-0.000}$	$0.29^{+0.01}_{-0.01}$	⋯
149.896	2.237	$1.187^{+0.001}_{-0.005}$	$13.67^{+0.02}_{-0.06}$	43	1/7	$0.034^{+0.008}_{-0.000}$	$0.13^{+0.01}_{-0.02}$	⋯
149.998	2.664	$1.213^{+0.011}_{-0.014}$	$13.65^{+0.12}_{-0.10}$	27	0/3	$0.014^{+0.007}_{-0.005}$	$0.48^{+0.15}_{-0.04}$	20130
149.700	2.014	$1.236^{+0.007}_{-0.007}$	$13.53^{+0.06}_{-0.09}$	204	5/19	$0.095^{+0.000}_{-0.019}$	$0.05^{+0.02}_{-0.02}$	⋯
149.727	2.008	$1.233^{+0.004}_{-0.007}$	$13.59^{+0.12}_{-0.07}$	292	8/35	$0.111^{+0.001}_{-0.019}$	$0.08^{+0.02}_{-0.02}$	⋯

Table 1
(Continued)

R.A. (J2000) (1)	Decl. (J2000) (2)	$z_{\rm phot}$ (3)	$\log(M_{200}/M_\odot)$ (4)	$N_{\rm mem}$ (5)	$N_{\rm outlier}/N_{\rm spec}$ (6)	FoF Fraction (7)	QF (8)	ID (9)
150.586	1.963	$1.271^{+0.005}_{-0.004}$	$13.85^{+0.05}_{-0.05}$	106	2/4	$0.037^{+0.000}_{-0.000}$	$0.11^{+0.02}_{-0.05}$	⋯
149.995	2.685	$1.290^{+0.006}_{-0.010}$	$13.62^{+0.16}_{-0.13}$	49	0/0	$0.129^{+0.026}_{-0.009}$	$0.10^{+0.02}_{-0.01}$	⋯
150.247	2.698	$1.275^{+0.003}_{-0.007}$	$13.69^{+0.17}_{-0.01}$	94	0/4	$0.159^{+0.000}_{-0.039}$	$0.04^{+0.02}_{-0.00}$	20174
149.950	2.547	$1.290^{+0.004}_{-0.006}$	$13.38^{+0.07}_{-0.11}$	46	2/4	$0.064^{+0.015}_{-0.001}$	$0.03^{+0.00}_{-0.02}$	⋯
149.945	2.652	$1.294^{+0.003}_{-0.008}$	$13.43^{+0.06}_{-0.04}$	205	2/7	$0.083^{+0.000}_{-0.017}$	$0.05^{+0.02}_{-0.00}$	⋯
149.947	2.634	$1.298^{+0.003}_{-0.009}$	$13.57^{+0.04}_{-0.03}$	89	1/4	$0.097^{+0.000}_{-0.017}$	$0.06^{+0.03}_{-0.01}$	⋯
149.884	2.674	$1.364^{+0.014}_{-0.006}$	$13.28^{+0.40}_{-0.29}$	37	0/1	$0.056^{+0.011}_{-0.011}$	$0.04^{+0.01}_{-0.07}$	⋯
149.817	2.017	$1.345^{+0.007}_{-0.003}$	$13.40^{+0.03}_{-0.03}$	23	6/7	$0.026^{+0.000}_{-0.006}$	$0.10^{+0.00}_{-0.00}$	⋯
149.815	1.888	$1.395^{+0.008}_{-0.005}$	$13.56^{+0.03}_{-0.09}$	46	3/5	$0.038^{+0.006}_{-0.000}$	$0.08^{+0.00}_{-0.05}$	20134
150.220	1.806	$1.393^{+0.006}_{-0.005}$	$13.41^{+0.18}_{-0.04}$	48	3/5	$0.037^{+0.000}_{-0.010}$	$0.05^{+0.02}_{-0.01}$	⋯
149.856	2.125	$1.397^{+0.003}_{-0.010}$	$13.62^{+0.01}_{-0.03}$	25	4/6	$0.025^{+0.006}_{-0.000}$	$0.11^{+0.02}_{-0.04}$	⋯

Notes. The full table is available online.

We list (columns (1)–(3)) the center of R.A., decl., photometric redshift, column (4) the halo mass estimated from the scaling relation with X-ray groups, column (5) the number of member galaxies, column (6) the number of photometric redshift outliers over the number of members with spectroscopic redshifts, column (7) FoF fraction, column (8) quiescent galaxy fraction, and column (9) the `ID_COSMOS` in the X-ray galaxy group catalog (G. Gozaliasl et al. 2019) if the cluster candidates are matched within $1h^{-1}$ Mpc and $|\Delta z| \leqslant 0.03(1+z)$.

(This table is available in its entirety in machine-readable form in the online article.)

we try the number of least connected redshift bins from 1 to 5, the use of more than three connected bins produces the smallest fraction of separate structures that are misidentified as clusters.

In addition, 27 out of 68 cluster candidates are matched with the X-ray galaxy group catalog (G. Gozaliasl et al. 2019). The X-ray groups that are not identified in this study include only a small number of member galaxies. On the contrary, the cluster-finding method based on overdensities cannot detect sparsely distributed members or a small number of members that have low overdensity significances as shown in the upper panel of Figure 3. Since X-ray groups are known to be biased to a more dynamically relaxed system than optically selected groups (E. O'Sullivan et al. 2017; L. Lovisari et al. 2021), we can speculate that our samples include overdensities not fully collapsed. The X-ray groups that are not detected in our samples with significant overdensities are all located near the survey edges (<1 Mpc) and bright source masks.

We estimate cluster halo masses (M_{200}) using the total stellar mass of member galaxies. To calibrate the mass estimator based on the total stellar mass, we compared the total stellar mass of member galaxies from this work to the X-ray-derived halo mass from G. Gozaliasl et al. (2019). The X-ray halo masses in the G. Gozaliasl et al. (2019) data are derived from the X-ray luminosity–halo mass relation with weak-lensing calibration from A. Leauthaud et al. (2010). Note that their mass-to-X-ray luminosity relation suggests a scatter in $\log(M_{200})$ of about 0.2 to 0.3. Here, the total stellar mass is defined as the sum of stellar masses above $10^{8.75}\,M_\odot$. Figure 3 compares the total stellar masses and the X-ray halo masses of clusters, showing a broad correlation between the two quantities. The fitting result between the X-ray halo mass and the stellar mass sum shows $M_{200} \propto 67.5^{+7.8}_{-7.0} \times$ total stellar mass. The derived halo masses are listed in Table 1. We note that we will use the terms "overdensity" and "galaxy cluster" interchangeably for the cluster candidates.

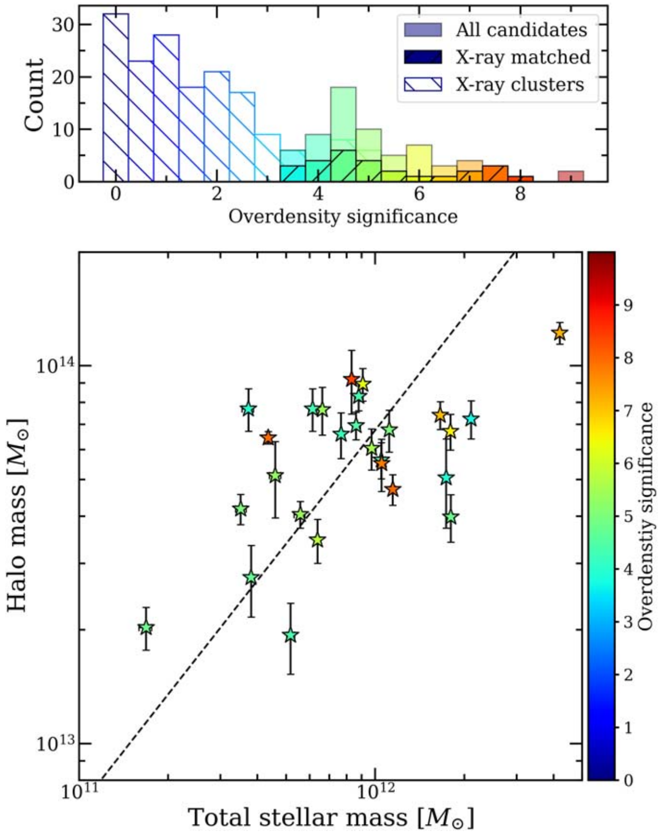

Figure 3. The comparison of cluster candidates found in this study and confirmed in the X-ray observation. The overdensity significance represents the number of standard deviations by which the density field deviates from its mean. Upper panel: the clusters that we identify have significant overdensities by definition, while X-ray groups are more likely to be less dense and comprise a small number of member galaxies. Lower panel: the matched clusters show a statistical correlation (Pearson correlation coefficient = 0.55) between the total stellar mass of member galaxies and halo mass estimated from X-ray detected groups. The best-fit linear regression between the two masses among cluster candidates is displayed as a black dashed line.

3. Results

3.1. Galaxy Evolution from the Star-forming to Quiescent Phase

A quiescent galaxy is defined as a galaxy that satisfies Equation (1) where $t(z)$ [yr^{-1}] is the age of the Universe at redshift z (M. Damen et al. 2009; S.-K. Lee et al. 2015),

$$\mathrm{sSFR} < 1/3t(z). \quad (1)$$

This definition takes into account the evolution of the specific star formation rate (sSFR) as a function of redshift and specifies quiescent galaxies as those that have relatively low sSFRs at a given redshift. We adopt sSFR values derived from SED fitting with `LePHARE`.

Alternatively, it is also possible to use the color plane to select the passive galaxies. For example, quiescent galaxies can be identified by a two-color selection *UVJ* method (I. Labbé et al. 2005; S. Wuyts et al. 2007; R. J. Williams et al. 2009). COSMOS2015 (C. Laigle et al. 2016) and COSMOS2020 (J. R. Weaver et al. 2022) adopted the NUV$-r^+$ versus r^+-J criteria where quiescent galaxies meet the conditions NUV$-r^+ > 3.1$ and NUV$-r^+ > 3(r^+-J) + 1$. This method is known to avoid a mix between quiescent galaxies and dusty star-forming galaxies. However, some of the quiescent galaxies at higher redshifts are still misclassified as star-forming galaxies because of uncertainties in their rest-frame colors (J. R. Weaver et al. 2022). Since the classification from both color and sSFR criteria exhibits a nearly identical result, our study leans toward classifying galaxies based on the sSFR for consistent comparison with L19. However, care should be taken with the sSFR from SED fitting, given its systematic scatter and bias over time (O. Ilbert et al. 2015; C. Laigle et al. 2019).

We investigate the difference between the results based on color and sSFR selection. Among the 86,289 galaxies more massive than $10^{8.99} M_\odot$ at $0.1 \leqslant z \leqslant 1.4$, we find 14,052 quiescent galaxies using the color selection and 17,777 using the sSFR selection. Notably, 95.3% (13,392/14,052) of the quiescent galaxies identified with the color selection are also flagged as quiescent based on the sSFR criterion in this study. The rest (660/14,052) are situated near the sSFR selection cut. Similarly, galaxies categorized as quiescent only through the sSFR (4385/17,777) are found located near the near-UV (NUV)$-r^+$ versus r^+–J color selection boundary. Of those, 3561/4385 are residing in the color space of star-forming galaxies within 0.1 dex from the selection cut. We tried another selection criterion, $\log(\mathrm{sSFR}) < \log(\mathrm{sSFR_{MS}}) - 0.6$ (K. E. Whitaker et al. 2012), where $\mathrm{sSFR_{MS}}$ is the sSFR [yr^{-1}] of the main sequence from J. S. Speagle et al. (2014). Only 19/17,777 quiescent galaxies based on the sSFR selection are regarded as star forming and vice versa 926/17,415, showing that our criterion is nearly identical to the criterion of $\log(\mathrm{sSFR}) < \log(\mathrm{sSFR_{MS}}) - 0.6$.

In other words, most galaxies flagged as quiescent galaxies by only one of the selection methods are marginally missed by the other. The three selection methods select galaxies with very similar properties, with a slight difference in selection boundary. Therefore, we suggest that our analysis is not sensitive to the selection method. We adopt the sSFR method as justified above, and conducted the same analysis for the NUV$-r^+$ versus r^+-J and sSFR $< 10^{-11}$ yr galaxy classifications. The results are nearly identical, so we will present only the results based on the sSFR-based galaxy classification.

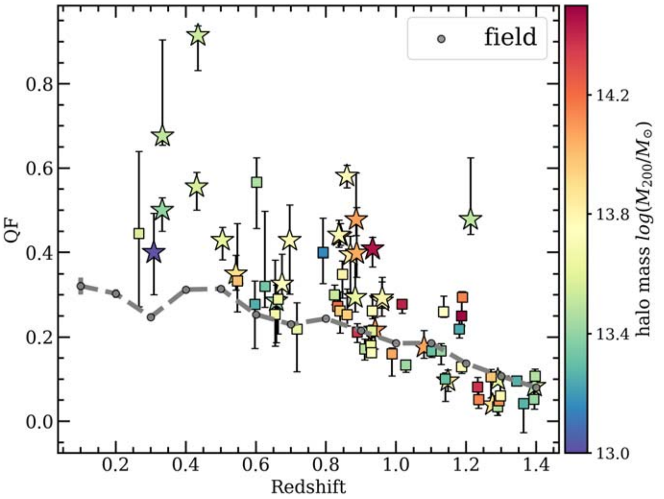

Figure 4. The distribution of quiescent galaxy fraction and redshift in the mass-limited sample. The error bars represent the 68% confidence interval obtained from 1000 iterations of determining the membership by adding the error to the redshift center of the cluster. The errors follow a normal distribution $N(0, \sigma(1+z))$, where $\sigma(1+z)$ corresponds to the photometric redshift uncertainty at a given redshift. For comparison, the quiescent galaxy fraction from the field is overlaid with a dashed line.

The quiescent galaxy fraction, hereafter abbreviated as QF, denotes the number of quiescent galaxies over the total number of member galaxies. We use the QF as an indicator of star formation activity in galaxy clusters since other measures, such as the total or median SFR, can be easily biased by the amount of dust extinction, which is not well constrained without deep infrared data. Meanwhile, the fractional parameter QF cancels out this effect and provides a more consistent metric regardless of the different assumptions involved in calculating the SFR. Figure 4 shows QFs in galaxy clusters as a function of redshift. As the redshift increases, the QF decreases, consistent with the Butcher–Oemler effect (H. Butcher & A. J. Oemler 1978). The intuition of the web-feeding model can be found here from the distribution of varying QF. At a given redshift and halo mass bin, the QFs of galaxy clusters have a wide range, which hints at the role of the environment, which influences the star formation activity or other physical parameter dependence.

3.2. Reliability of 2D Density Field

As a quantitative proxy of the connected structure to a galaxy cluster, we define the term *friends-of-friends fraction* (hereafter FoF fraction) as the ratio between the total area of the 2σ-level projected overdense regions connected with a 2 Mpc linking length by the FoF algorithm (M. Davis et al. 1985; red region in Figure 5) and the projected area within a radius of 10 Mpc from the cluster (gray+red+pink region). In simple terms, this FoF fraction characterizes the channel where large-scale cosmic web feeding can take place. Because we are interested in the intercluster scale, we restrict our analysis to the environment within 10 Mpc. Additionally, we use 2 Mpc as the linking length, which aligns with the typical size of galaxy clusters and is short enough to account for interactions among galaxies or groups. We checked that the variation of linking length (0.5, 1.0, 1.5, 2.0 Mpc) does not significantly change the overall results.

We note that there have been various methods to measure the large-scale cosmic web (e.g., T. Sousbie 2011; M. Cautun et al. 2013; M. Alpaslan et al. 2014; E. Tempel et al. 2014;

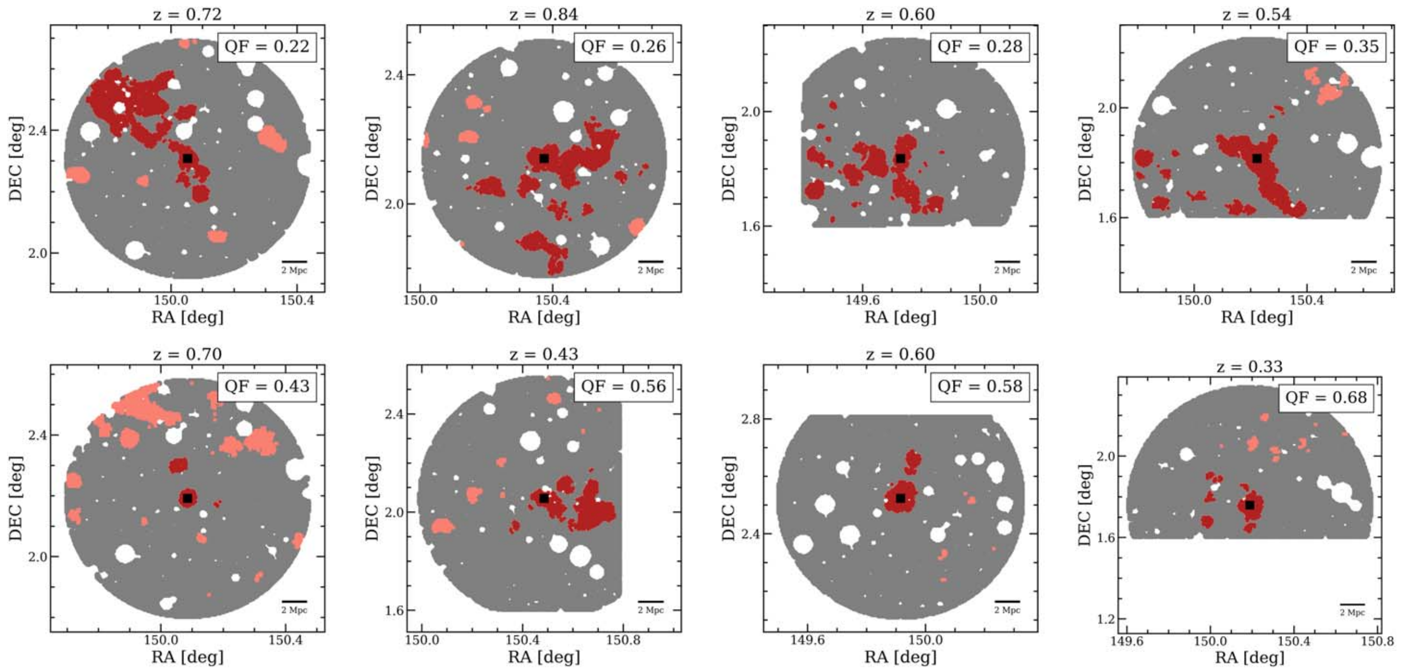

Figure 5. Examples of overdense areas showing how the FoF fraction is defined. Each panel displays overdensities (red region) connected to host cluster candidates (filled black square) in increasing order of QF (left to right). The FoF fraction is defined as the ratio of the red area to the whole area (gray+red+pink areas). Unconnected overdensities within a 2 Mpc linking length are depicted in the pink region.

N. I. Libeskind et al. 2018). Admittedly, there may be better ways to analyze the effect of the web-feeding model than the FoF fraction. However, we decided to adopt the FoF fraction for comparing our results with L19 in a consistent way by using the same metric. Since defining the large scales is subject to the choice of the measurement method, uniformly gauging the impact of the scales of our interest (intercluster ∼Mpc) is challenging. With a cosmological simulation, we confirm that galaxies and small groups are infalling following the 2σ overdensities connected to the host cluster in Section 4.2. In the future, we hope to explore if there are better ways to calculate the web-feeding trend.

To sum up, the FoF fraction indicates the volume (area) of the reservoir from which infalling galaxies, groups, or cold gas, if it exists, originate. We refer to these infalling components as *infallers* and expect them to impact the QF. The precise influence of infalling galaxies and cold gas on the increase in star-forming galaxies in clusters is not clear. We will discuss the role of gas on cluster galaxies in Section 4.2. Therefore, we refer to all the different ingredients fueling a cluster to keep the QF at a low value as infallers for simplicity.

Before testing the web-feeding model, we check if the 2D projected structures can represent actual 3D structures. Using the same galaxy light-cone mock catalog (A. I. Merson et al. 2013) employed to verify the cluster-finding method, we calculate the relationship between the FoF fraction derived from (1) a cylindrical region, with a projected physical radius of 10 Mpc and a height corresponding to the photometric redshift uncertainty $0.01(1+z)$ and (2) a spherical region within a physical radius of 10 Mpc from the cluster center. Figure 6 shows a moderate correlation between the 2D and 3D FoF fractions with a correlation coefficient of 0.700. Several previous studies (e.g., B. Darvish et al. 2017; C. Laigle et al. 2018) have also demonstrated that 3D cosmic web can be reliably traced from 2D counterparts up to $z \sim 1$ with a photometric redshift uncertainty of the order of $0.01(1+z)$.

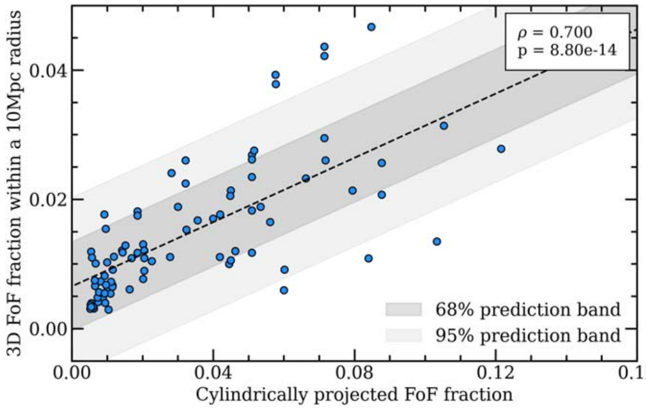

Figure 6. The x-axis denotes the 2D projected cylindrical FoF fraction in the light-cone mock catalog (A. I. Merson et al. 2013) derived with the same method for COSMOS2020. On the other hand, the y-axis denotes the 3D spherical FoF fraction, taking into account a physical distance of 10 Mpc in the same mock data. They exhibit a general correlation within the 95% prediction level. The Pearson correlation coefficient is ρ and p-value p. The best-fit linear regression line is shown as a dashed line.

3.3. Web Feeding in the COSMOS Field

Figure 7 shows the relationship between the FoF fraction and the QF covering the overall redshift range ($0.1 \leqslant z \leqslant 1.4$). The lower FoF fractions exhibit a broad range of QFs whereas higher FoF fractions are mostly associated with low QFs. The Pearson correlation coefficient for the FoF fraction and the QF is −0.401. Even though the correlation itself is not strong, it remains significant given the p-value (0.0007) and the general trend is consistent with the result of L19. This trend is visually demonstrated in Figure 5, where we show the density map with the cluster QF and the connected LSS are indicated. In the upper panels, clusters with lower QFs are shown to have LSSs connected to them (i.e., higher FoF fraction). Similarly, clusters with higher QFs are found to be relatively isolated (i.e., lower

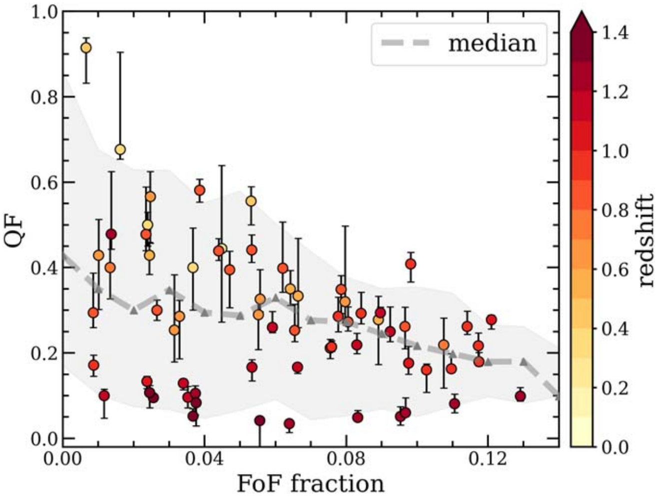

Figure 7. The QF as a function of the FoF fraction for the total 68 galaxy clusters found in the COSMOS field. The color code denotes the redshift of a given cluster. The gray dashed line is plotted as the median QF at a given FoF fraction with a 1σ confidence level (gray shade).

FoF fraction) in the lower panels. This supports the web-feeding effect of the large-scale cosmic web on star formation activity in galaxy clusters. Therefore, galaxy clusters with low QFs generally populate largely connected environments rather than isolated areas.

3.3.1. The Effect of Redshift and Halo Mass

While these results are consistent with the web-feeding model, it is well known that the QF is also dependent on the cluster halo mass and environment (e.g., A. R. Wetzel et al. 2012). In order to separate the effect of redshift evolution and halo mass, we divided the redshift bins into four intervals ($0.3 \leqslant z < 0.6$, $0.6 \leqslant z < 0.9$, $0.9 \leqslant z < 1.2$, $z \geqslant 1.2$) as shown in Figure 8. For the two lower redshift bins at $0.3 \leqslant z < 0.6$ and $0.6 \leqslant z < 0.9$, the correlation between the FoF fraction and QF is more pronounced than the whole sample, with the correlation coefficients ρ of -0.790 and -0.492, respectively. We will discuss the opposite trend at $0.6 \leqslant z < 0.9$ by constraining the halo mass. On the other hand, no clear FoF fraction dependence on the QF appears for higher redshift bin ($z \geqslant 1.2$). At this epoch, the growth of the overdensities is not as advanced as in those at lower redshifts where the trend of web feeding appears clearly. The other explanation is that most galaxies at high redshifts are not quenched yet unlike their counterparts at lower redshifts. In the earlier Universe, the star formation activity in cluster members is still comparable to that of field galaxies (e.g., M. Brodwin et al. 2013), demonstrating that the correlation between the QF and the FoF fraction does not stand out.

Following the nature of the web-feeding model, the accretion of galaxies is more likely to be strong at the site where the gravitational potential is the deepest. For the lower redshift bins at $0.3 \leqslant z < 0.6$ and $0.6 \leqslant z < 0.9$, we also examined how the FoF fraction versus the QF trend changes depending on the M_{200} values. The partial correlation coefficients ρ_h when fixing halo mass at a given redshift bin are -0.794 (p-value $= 0.009$) and -0.486 (p-value $= 0.013$), showing nearly identical correlation. The result suggests that the FoF fraction versus the QF correlation exists independent of the M_{200} dependence. While clusters lying at low redshift still follow the persistent relation with fixed halo masses, high-redshift clusters still do not show any such trend. At $0.9 \leqslant z < 1.2$, the statistical analysis indicates that the QF is not related to the FoF fraction when considering fixed halo mass, although a correlation is observed when halo mass is not constrained. Consistently, the anticorrelation trend becomes insignificant at higher redshift $z \geqslant 1.2$.

The observed web-feeding trend appears to diverge from the previous findings presented in E. Darragh Ford et al. (2019) and K. Kraljic et al. (2020), where central galaxies in groups or clusters connected to more filaments (with higher connectivity, indicative of the large-scale cosmic web) (S. Codis et al. 2018), are found to be less star forming. We confirm that passive central galaxies in our cluster candidates do not show larger FoF fractions than star-forming ones as suggested in E. Darragh Ford et al. (2019). E. Darragh Ford et al. (2019), relying on the `Horizon-AGN` simulation (Y. Dubois et al. 2014), speculated that groups with higher connectivity are more likely to have experienced a group major mergers in their past, which would have increased the connectivity (see also C. Gouin et al. 2021), and in the long term, quenched the central galaxy due to the activity of the central AGN (T. Di Matteo et al. 2005; Y. Dubois et al. 2016). We note however that the X-ray selection might be biased toward relaxed groups (e.g., E. O'Sullivan et al. 2017; L. Lovisari et al. 2021; R. Seppi et al. 2022) and concentrated structures containing an AGN (e.g., Y. Shen et al. 2007; S. Oh et al. 2014). In this sense, the COSMOS X-ray group sample might miss those groups/clusters that are either structures not fully collapsed, like protoclusters, or clusters specifically in the process of merging, and therefore containing galaxies with temporarily boosted star formation (e.g., P. Di Matteo et al. 2007; G. Martin et al. 2017). Indeed, only 10 of our clusters overlap with the groups in E. Darragh Ford et al. (2019). However, it is crucial to note that our investigations focus on the influence of the cosmic web extending beyond overdensity-based clusters ($\sim$10 Mpc) on member galaxies. It remains plausible that satellite galaxies maintain their star formation within relatively dense environments, while massive central galaxies are more prone to quenching (A. R. Wetzel et al. 2012; R. J. Smethurst et al. 2015; P. W. Hatfield & M. J. Jarvis 2017; S. V. Werner et al. 2022).

3.3.2. The Effect of Stellar Mass

Since the QF is also dependent on the stellar mass of galaxies with the QF being higher for higher M_* galaxies (e.g., Y.-j. Peng et al. 2010; N. Scoville et al. 2013; S.-K. Lee et al. 2015), we look into the QF versus the FoF fraction correlation further to see how the M_* dependence plays out in the correlation. To accomplish this, we examine the QF versus the FoF fraction trend by dividing the member galaxy sample by their M_*. Figure 9 presents the median QF and sSFR for member and field galaxies in stellar mass bins at a given redshift bin, comparing those in *connected* clusters, *isolated* clusters, and in the *field*. Here, the connected clusters are defined as those with an FoF fraction larger than the median in the corresponding redshift bin, isolated as those with an FoF fraction less than the median and field as those that do not belong to clusters or 2σ overdensities.

The upper panels of Figure 9 illustrate that the QFs of isolated clusters are generally higher across most M_* values than those of connected clusters at $z < 0.9$. Similarly, the sSFRs

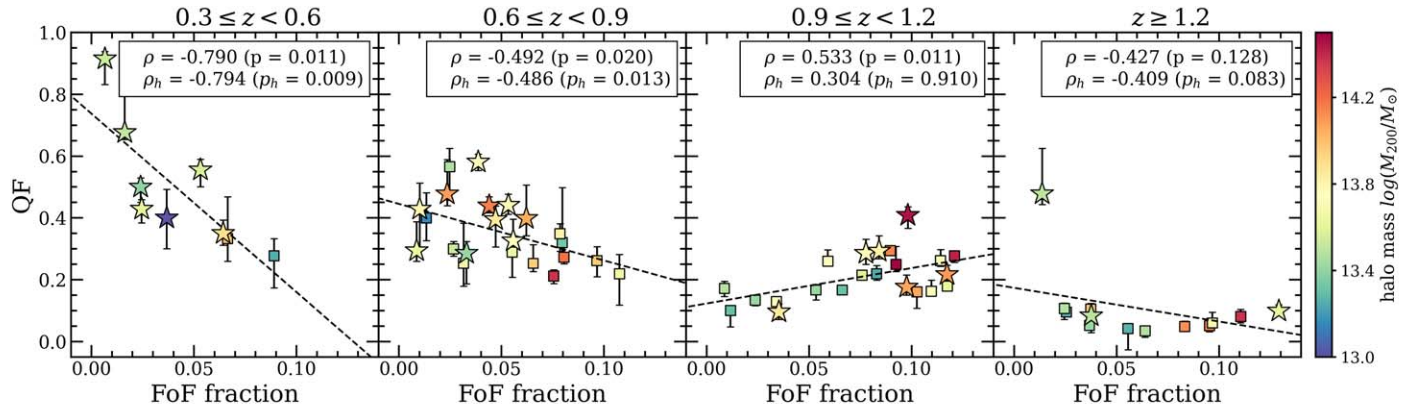

Figure 8. The anticorrelation between the QF and FoF fraction in 4 redshift bins. The Pearson correlation coefficient and its associated p-value are denoted as ρ and p_h, respectively, where the subscript h signifies fixed halo masses. The halo mass is represented as a color of marker. The star-shaped markers correspond to the clusters that have been detected in the X-ray group catalog (G. Gozaliasl et al. 2019) while those in square shape are candidates found based on photometric redshifts in this study.

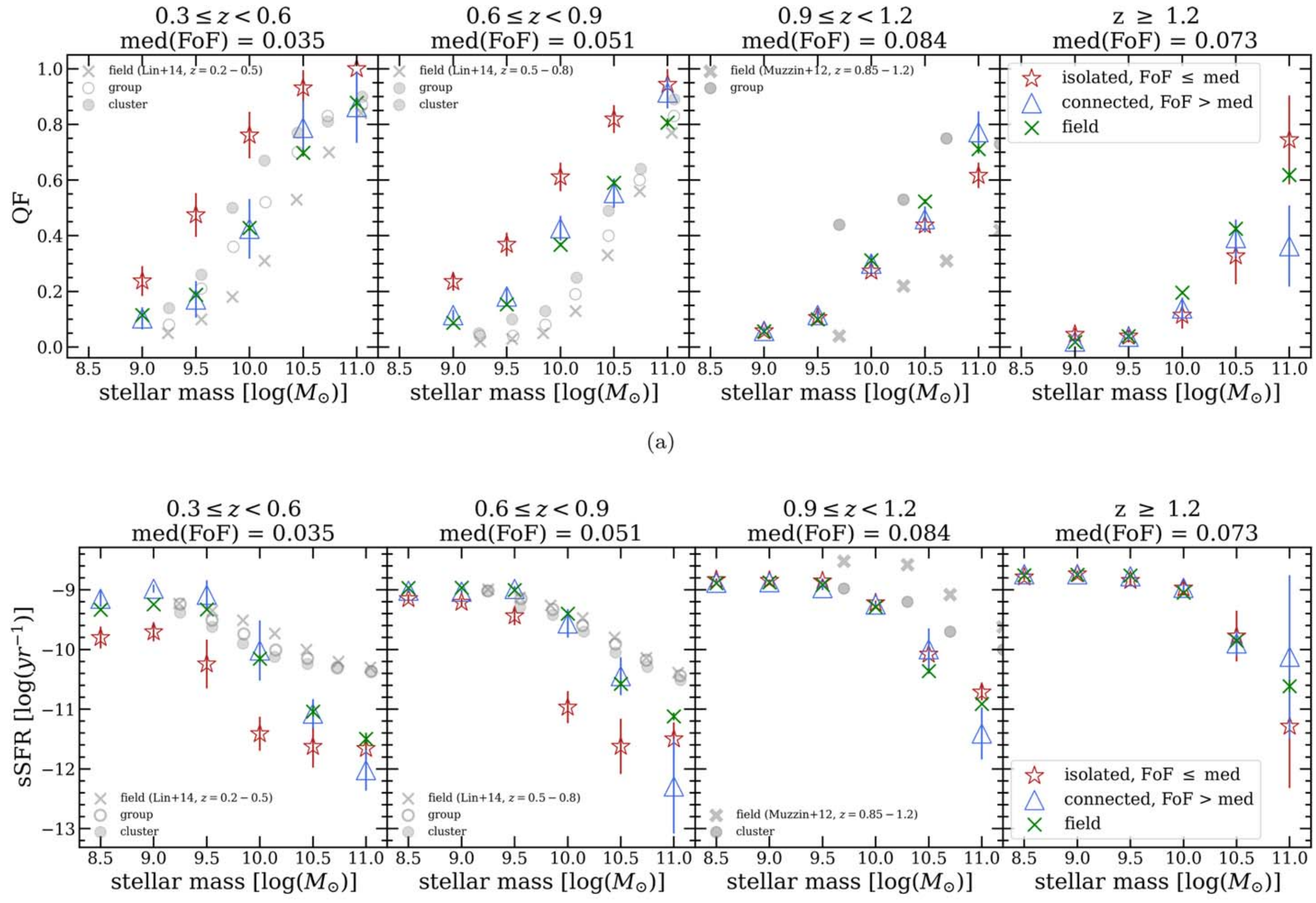

(a)

(b)

Figure 9. The median QF (upper panel) and median sSFR (lower panel) in each stellar mass bin of member galaxies. The member galaxies in clusters with FoF fractions larger than the median at a given redshift bin (open red star) are more actively forming stars than those in clusters with lower FoF fractions (open blue triangle). The filled green cross represents the case of field galaxies that are residing in the area with density $\leqslant 2\sigma$ for reference. The observational data from other literature (A. Muzzin et al. 2012; L. Lin et al. 2014) are overplotted in gray points. Here, we only compare the face values of the sSFR and the QF to see if their general trends with regard to stellar masses are consistent. Note that the criteria of quiescent/star-forming galaxies, environment (field, group, and cluster), and initial mass function (IMF) models are different between studies.

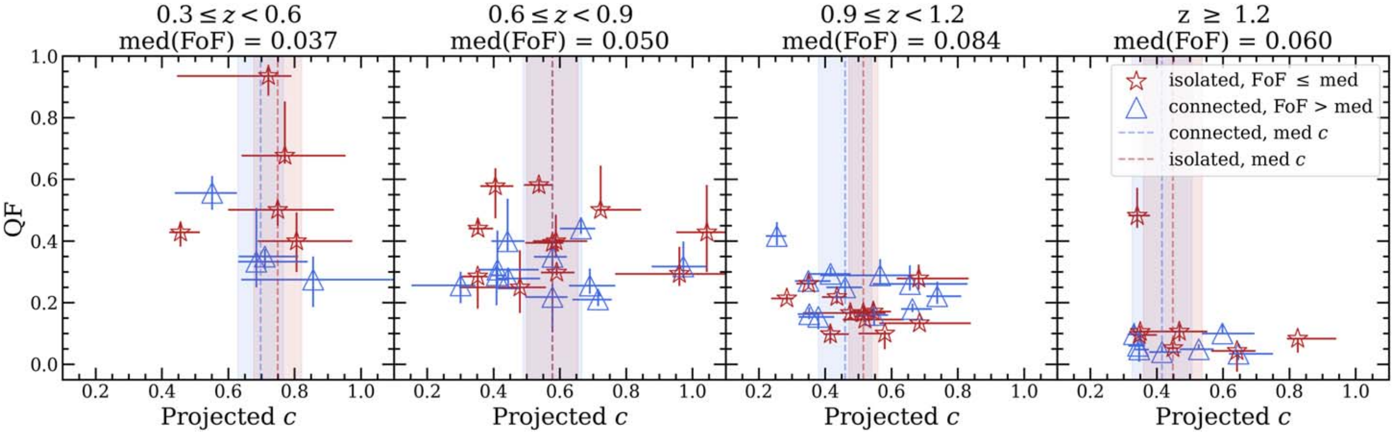

Figure 10. The comparison of concentration parameters and QFs in connected (the open blue triangles) and isolated clusters (the filled red stars). No notable difference for c is found between the isolated and connected clusters.

Table 2
The Median Projected Concentration Parameters and 1σ Confidence Interval with Various FoF Fractions and Redshifts

	Median Projected Concentration Parameter	
Redshift	Connected	Isolated
$0.3 \leqslant z < 0.6$	0.70 ± 0.07	0.75 ± 0.07
$0.6 \leqslant z < 0.9$	0.58 ± 0.09	0.58 ± 0.08
$0.9 \leqslant z < 1.2$	0.46 ± 0.08	0.51 ± 0.04
$z \geqslant 1.2$	0.42 ± 0.09	0.45 ± 0.09

tend to have lower values for isolated clusters compared to connected clusters (the lower panel of Figure 9). The connected clusters have QFs and sSFRs similar to galaxies in the field. However, beyond $z \geqslant 0.9$, the QF distribution between the field, isolated, and connected clusters disappears. A similar trend is found for the sSFR of member galaxies. These results confirm the correlation between the QF and the FoF fraction at $z \lesssim 0.9$ regardless of M_*, as expected from the web-feeding model.

Notably, field galaxies show star formation activities similar to galaxies in connected clusters. The similarity in the QF or sSFR between field galaxies and connected clusters reflects the influence of infalling galaxies keeping the QF relatively low. Such galaxies would be eventually quenched. A similar trend can be found for cluster and field galaxies studied in L. Lin et al. (2014).

3.3.3. Concentration Parameter

The physical difference between connected and isolated clusters is also investigated with projected concentration parameters c defined as the ratio of the area where 30% and 70% of members reside. The projected concentration parameter serves as a practical proxy of the concentration parameter from the Navarro–Frenk–White (NFW) density profile (J. F. Navarro et al. 1997) when only photometric redshifts are available. In Figure 10, we calculate the projected concentration parameters for each redshift bin and present those values in Table 2.

Across all four redshift bins, no significant difference between the projected concentration parameters in connected and isolated clusters is observed. This tendency is consistent with the findings of L19, where the correlation between the QFs and c is weak. If the clusters with high FoF fractions are contaminated more by surrounding density structures, we expect to find a difference in the concentration parameter as a function of FoF fraction values. No strong correlation with c and the FoF fraction in Figure 10 and Table 2 assures that the cluster selection is not biased by the surrounding structures.

3.4. Comparison with the `IllustrisTNG` Hydrodynamical Simulation

To better understand the web-feeding model and the related results from the observation in the previous section, we use the `IllustrisTNG` simulation (D. Nelson et al. 2018; V. Springel et al. 2018). `TNG300` has a simulation volume with a box size of 300 Mpc on each side, providing a statistically robust sample of galaxy clusters. The group catalog in `IllustrisTNG` identifies halos using a standard `FoF` algorithm (M. Davis et al. 1985) with a linking length parameter of $b = 0.2$. Here, b is a dimensionless free parameter that scales the mean inter-particle distance of collapsed halo particles relative to that of the global distance. The commonly adopted value of $b = 0.2$ corresponds to a density contrast between halo density and the global mean density to be 200 (S. More et al. 2011). Our analysis focuses on halos with M_{200} (`Group_M_Crit200`) more massive than $10^{13}\,M_\odot$, which matches the range of cluster masses observed in COSMOS2020. We also use subhalos derived from the `Subfind` algorithm, which relies on all particle species to identify galaxies (V. Springel et al. 2001; K. Dolag et al. 2009) whose stellar masses within twice the half-mass radius are more massive than $10^{8.5}\,M_\odot$ (see, e.g., A. Pillepich et al. 2018 for the description of the algorithm). This choice is consistent with a mass complete sample in observation and varying the minimum stellar mass from $10^{8.5}$ to $10^{9}\,M_\odot$ does not result in different results. We describe details on how the `TNG300` data are analyzed to interpret the observational results in the Appendix.

We check if the web-feeding trend similar to the result found from COSMOS2020 can be replicated in simulation. The relation between the FoF fraction and the median QF is shown in Figure 11. The FoF fraction and the QF do not seem to be related even after dividing galaxy clusters into different halo masses or high and low-concentration categories. But, the QF increases with halo mass regardless of redshifts. We compare QFs as a function of stellar mass for galaxies in both isolated and connected clusters in Figure 12. In the simulation results, the QFs of isolated clusters are nearly identical to those of connected clusters, which contradicts the observational results

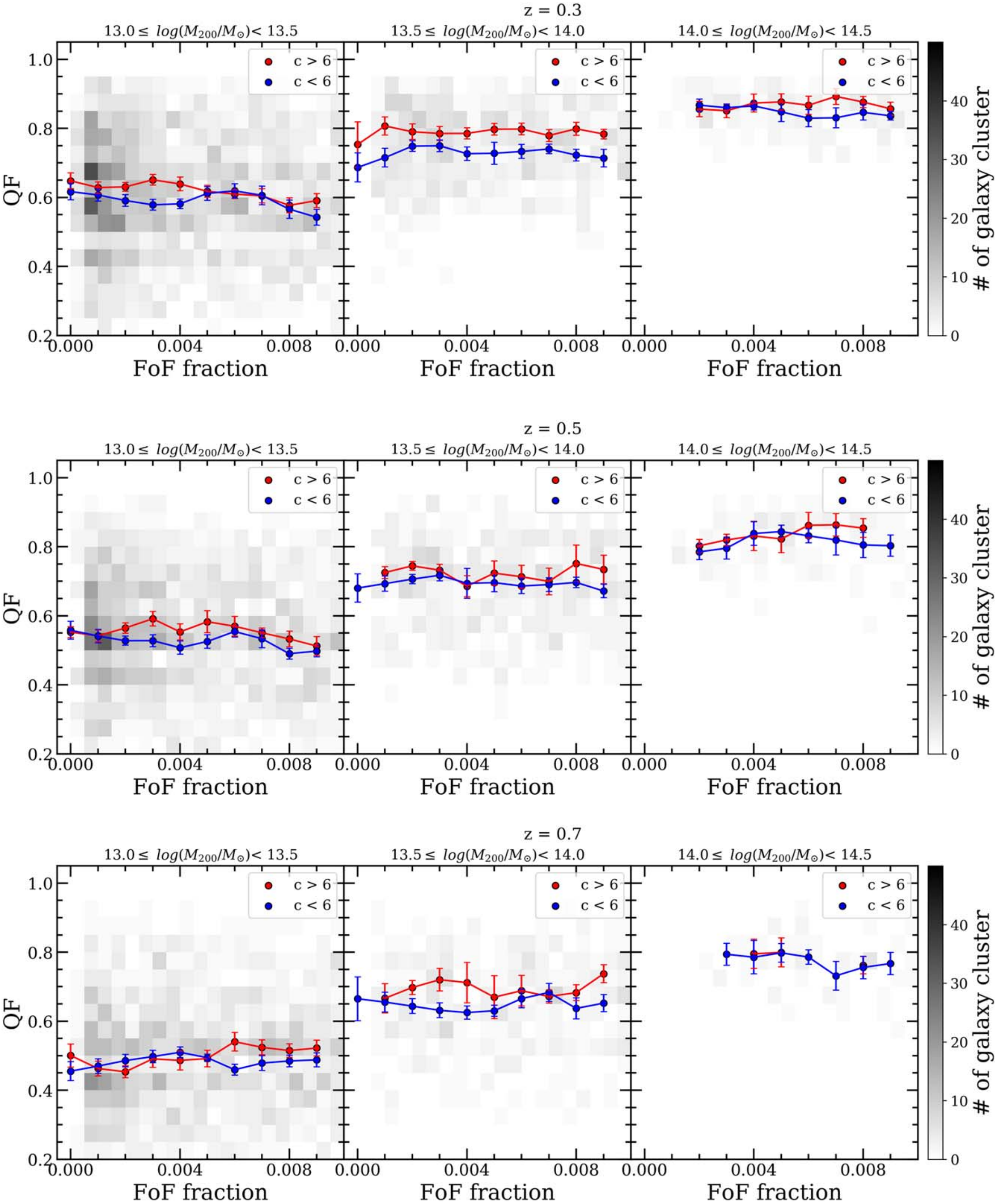

Figure 11. The median QF as a function of the FoF fraction in the `TNG300` simulation. The concentration parameter *c* fitted from the NFW profile (J. F. Navarro et al. 1997) is obtained from D. Anbajagane et al. (2022).

in Figure 9. An obvious discrepancy between simulation and observation may be found in the distribution of the QF in stellar mass bins (Figure 12). In contrast to the increasing trend in the QF with increasing stellar mass, the QF in low stellar mass bins tends to be measured higher. We will speculate on the possible causes for the discrepancy in the next section.

4. Discussion

4.1. Discrepancy between Observations and Simulation

Considering that the 3D FoF fraction is a more accurate representation of the surrounding LSSs than the 2D FoF fraction, we expect that the QF–FoF fraction correlation would

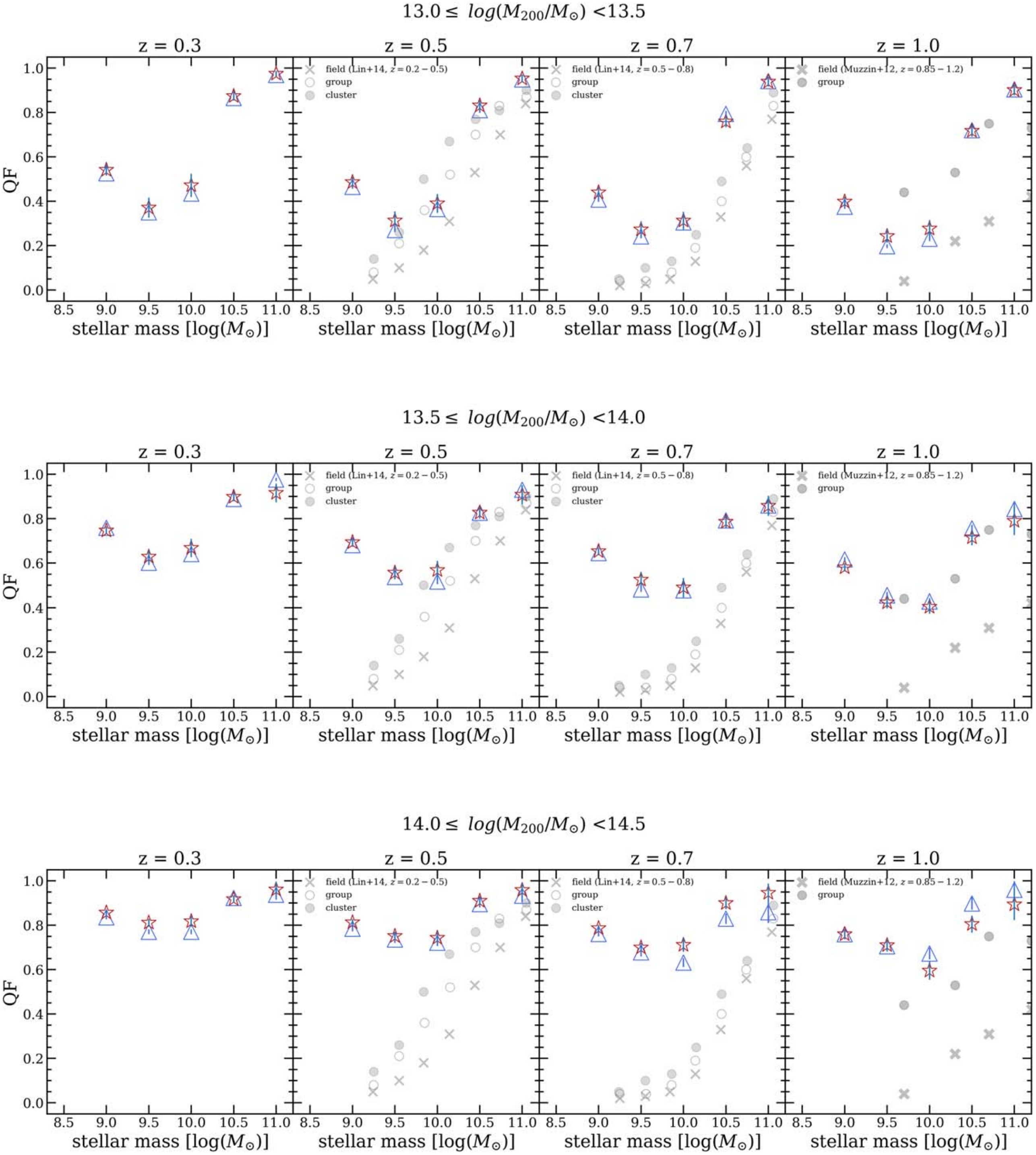

Figure 12. The median QF in stellar mass bins of member galaxies in the `TNG300` simulation. The QFs of isolated clusters are nearly identical to those in connected clusters over the entire stellar mass bin and regardless of the halo mass. For comparison, the observational data are shown in gray symbols, where the meanings of the points are the same as those in Figure 9.

be weakened when using the 2D FoF fraction with a sizable scatter to trace these structures in comparison to the same relation explored in 3D as in the simulation data. In reality, we find an opposite trend as shown in the previous section. Therefore, we exclude the increased scatter in the 2D FoF fraction due to moving from the 3D to the 2D distribution for the possible reasons for the discrepancy. Furthermore, we confirm no correlation in `TNG300` between QFs and FoF fractions even when we calculate the 2D FoF fraction with the projected 3D FoF fraction and repeat the same analysis.

The tension in the results between the observations and the `TNG300` simulation may arise from both observations and simulation. We briefly suggest the possible causes that might drive the disparity.

4.1.1. Caveats from the Observation

It is possible that clusters and their member galaxies, determined from photometric redshifts, could suffer from interlopers (R. J. Brunner & L. M. Lubin 2000; J. Benjamin et al. 2010; G. M. Shattow et al. 2013). While our fiducial choice of photometric redshift uncertainties $\sim 0.01(1+z)$ is obtained from the most up-to-date catalog at the moment, the physical distance corresponding to this error is ∼20 Mpc at $z \sim 1$, which is much larger than the typical cluster size. Hence, one may argue that the web-feeding trend could be an outcome of the line-of-sight structures overlapping with each other. We prepared the simulation data as similar as possible to the observational data by adding scatters in redshifts to see if we could reproduce the web-feeding result. However, this test did not produce an artificially created web-feeding effect, suggesting that the line-of-sight effect combined with redshift uncertainty is not likely to solve the tension between observation and simulation.

Finally, the COSMOS2020 field size is smaller than the `TNG300` simulation box size, so the cosmic variance may be in play (R. Bordoloi et al. 2010; J. A. Newman & D. Gruen 2022). Such a case can be tested in the future by examining the data set much wider than COSMOS2020.

4.1.2. Caveats from the Simulation

The resolution limit in large-volume cosmological simulation could be a problem causing the tension. The studies from M. Donnari et al. (2019, 2021b), and M. Donnari et al. (2021a) suggest that QFs in simulation can deviate from observations at the high-mass and low-mass ends and depending on the halo mass definitions or even QF definitions by 10%−40%. In our case, the QF of halos in `TNG300` is consistent with the observations at $M_* > 10^{9.5}\,M_\odot$ but at lower masses, it deviates from the observation significantly. We repeat our analysis by restricting the galaxy's stellar mass to $M_* > 10^{9.5}\,M_\odot$ but unfortunately that does not reveal a correlation between the QF and FoF fraction.

Matching our cluster samples of interest with the simulation is also not trivial. Since our cluster candidates are obtained based on overdensities, we selected samples experiencing various relaxation stages from extended to concentrated structures (Y.-K. Chiang et al. 2013). On the contrary, in `TNG300`, the clusters are detected with the FoF algorithm, finding uniform candidates whose density is 200 times larger than the global one. Due to the difficulties of matching precise definitions of clusters, various quenched fractions are also found even among observations themselves (G. M. Shattow et al. 2013; S. I. Muldrew et al. 2015).

In short, the web-feeding trend observed in COSMOS2020 does not appear in the TNG300 simulation. Future surveys with more accurate redshifts will reduce the uncertainty of cosmic structures and minimize projection effects. The availability of high-resolution cosmological simulation, preferentially the one including a light-cone data set, will also offer more improved pictures of the effect of LSSs on star formation in clusters of galaxies, enabling us to mimic the observed data and analysis in the same way. Given the current limitations, this aspect remains a topic for future analysis.

4.2. What Fuels the Galaxy Cluster?

Here, we focus on the infallers responsible for fueling the host cluster and their respective effects by tracing snapshots at different redshifts `TNG300`. By selecting clusters that are more massive than $10^{14}\,M_\odot$ at the present epoch, we track the member galaxies back in time to $z = 2$. For largely connected galaxy clusters to remain star forming or less quenched compared to isolated counterparts, the QF of infalling galaxies must be less than that of the host galaxy cluster. The QFs of prospective members, assessed at one snapshot just before their accretion, are depicted in Figure 13. Infalling galaxies embedded in halos more massive than $10^{12}\,M_\odot$ are classified as infalling groups, and otherwise, individual galaxies. Since not all the nearby galaxies surrounding a given halo infall into the galaxy cluster, we exclusively calculate the QF of infallers that would become member galaxies of the host cluster at the next snapshot (M. Donnari et al. 2021a; U. Kuchner et al. 2022; R. Haggar et al. 2023). As expected, the QFs of both infalling galaxies and groups are lower than the QF of the host cluster. For the case of infalling groups, *preprocessing* takes place and the star formation is quenched to a certain degree at the pre-infall stage (Y. Hashimoto 1998; A. Sengupta et al. 2022). The infalling individual galaxies have lower QFs than galaxies in infalling groups, while the number of galaxies in group-scale structures dominates the number of infallers compared to cluster members. The role of infalling groups on cluster evolution is also consistent with previous studies (S. L. McGee et al. 2009; M. Donnari et al. 2021a).

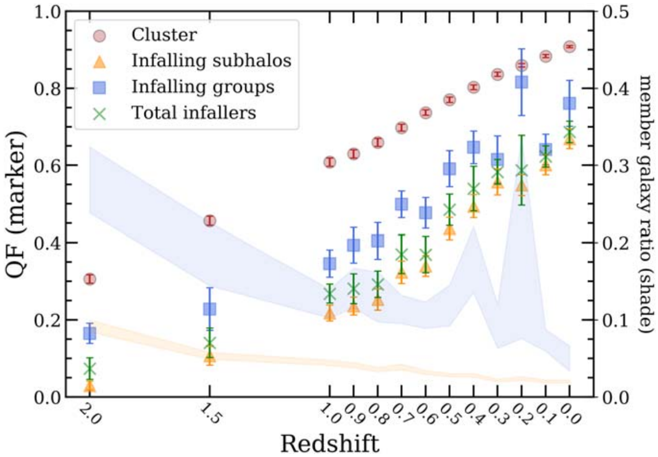

Figure 13. The median QF of host galaxy clusters (pink circle), galaxies in infalling groups (filled blue square), infalling galaxies (filled orange triangle), and total infallers (galaxies + groups, filled green cross) at a given snapshot (redshift). The member galaxy ratio, represented as blue (groups) and orange (galaxies) shades, shows the number of infalling galaxies/groups divided by the number of cluster members before the accretion of the galaxies/groups.

We do not explicitly address the case of cold gas accretion due to the lack of cold gas estimates in COSMOS. Nonetheless, previous studies hint at the role of cold gas accretion in fueling star formation activities within filaments and cluster environments. We introduce some examples as follows. From the xGASS survey (B. Catinella et al. 2010, 2013), S. Janowiecki et al. (2017) shows that central galaxies in low-mass groups tend to exhibit higher H I gas fractions and sSFR by 0.2 −0.3 dex than galaxies in isolation. They speculate that the H I gas reservoir of low-mass central galaxies is replenished through infalling gas along cosmic filaments and by the merging of gas-rich satellites. Moreover, in regions with moderate overdensities between field and cluster environments, small, gas-rich, and star-forming groups seem to represent an early stage of group evolution. The presence of cold gas and its effect on delayed quenching is also supported by zoom-in cosmological simulations with high resolution. S. Kotecha et al. (2022) investigate the impact of intracluster filaments using hydrodynamic zoom re-simulation of The Three Hundred project (A. Klypin et al. 2016; W. Cui et al. 2018). In the simulation, intracluster filaments enable a coherent and less disturbed gas flow, suppressing ram pressure and keeping galaxies forming stars. This shock property of gas can feed clusters through the cosmic web more smoothly (A. Rost et al. 2021; D. Galárraga-Espinosa et al. 2023; I. Vurm et al. 2023; A. M. Rost et al. 2024).

4.3. Can Other Processes Explain the Scatters in the Web-feeding Trend?

It is important to note that the web-feeding model could be an outcome of various quenching mechanisms acting in galaxy clusters at different evolutionary stages. The scatter in the correlation between FoF fractions and QFs suggests the involvement of other processes. One possibility is that a delayed quenching timescale might cause the population to diverge from the main correlation. For example, Figure 7 shows galaxy clusters with lower FoF fractions and lower QFs, deviating from the web-feeding trend. We suppose that the delay in quenching might allow isolated clusters to remain star forming temporarily after web detachment (A. R. Wetzel et al. 2013; D. S. Taranu et al. 2014; C. P. Haines et al. 2015; R. Foltz et al. 2018).

However, long after the web-feeding effect fades away, one may argue that hydrodynamical quenching processes are more prevalent in isolated clusters, where web feeding is less prominent. With limited gas reservoirs from the cosmic web, the effects of starvation or overconsumption can manifest more dramatically (S. L. McGee et al. 2014; M. L. Balogh et al. 2016). In dense environments like clusters, gravitational interactions can become more pronounced. As a result, an increased chance of mergers (L. Lin et al. 2014; H.-Y. Jian et al. 2017) and tidal stripping (A. Boselli et al. 2016; Y. Fang et al. 2016; E. L. Łokas 2020) could expedite quenching processes. But in such cases, the halo mass should be the main driver for the quenching, rather than the connection to the surrounding LSS.

5. Conclusion

We test the web-feeding model using the COSMOS2020 data and the `TNG300` simulation. Our analysis of the COSMOS field confirms that the large-scale cosmic webs surrounding the galaxy clusters and the star-forming activity are correlated to $z \lesssim 1$. By analyzing the simulation data, we suggest that the correlation possibly results from the infallers supplied by connected overdensities and feeding the galaxy clusters. Our results are summarized as follows:

1. We identify 68 galaxy overdensities from $z = 0.1$ to 1.4 in the COSMOS field. The halo masses are estimated to be in the range of $13.0 \leqslant \log(M_{200}/M_{\odot}) \leqslant 14.5$ by matching them with the X-ray group catalog from G. Gozaliasl et al. (2019).

2. We find that the QF decreases as redshift increases and halo mass decreases. Nevertheless, there remains a wide range of variation in the QF of galaxy clusters at a similar redshift and halo mass. The scatters can be at least partially explained by the correlation between the QF and FoF fraction at $z \lesssim 0.9$. For galaxy clusters at $z \lesssim 0.9$, the more connected area (higher FoF fraction) shows higher enhancement in star formation activity (lower QF), which is consistent with the expectation from the web-feeding model. The web-feeding model illustrates that the inflow of star-forming galaxies and groups from LSSs can keep a galaxy cluster active.

3. There is no remarkable correlation between the FoF fraction and QF at $z > 0.9$. The QFs of cluster members are comparable to those in the field, suggesting that either cluster members have not evolved sufficiently to be distinct from those in the field or that the identification of clusters and cluster members is challenging at the higher redshifts.

4. A complementary perspective is provided by our examination of simulation data. We track the time evolution of galaxy clusters with their surrounding environments using the `TNG300` simulation from the present epoch to $z = 2.0$. Unlike in COSMOS2020, no clear correlation between the QF and FoF fraction can be found. In the simulation, the cause of the discrepancy between the simulation and the observation results is unclear.

5. Using the simulation data, we examine the properties of infalling structures and their paths toward galaxy clusters. Infallers consist of individual galaxies and groups that have lower QF than the cluster to which they infall. These infallers follow the FoF overdensities and may contribute to keeping the QF of clusters low. Group-scale structures encompass the majority of infallers, while individual galaxies contribute to lowering the overall QF among infallers.

One limitation of this study is the use of photometric redshifts. Although photometric redshifts are deemed accurate enough for tracing LSSs, there is a potential for interlopers to contaminate the measurements of clusters and surrounding LSSs. Future studies, supported by a larger number of spectroscopic data, should be able to provide better insights into the connection between cluster star formation activities and surrounding environments.

Acknowledgments

This work was supported by the National Research Foundation of Korea (NRF) grants Nos. 2020R1A2C3011091 and 2021M3F7A1084525, funded by the Korean government (MSIT). We would like to thank the COSMOS Collaboration. This research was supported in part by grants NSF PHY-1748958 and PHY-2309135 to the Kavli Institute for Theoretical Physics (KITP). S.L. acknowledges support from a National Research Foundation of Korea (NRF) grant (2020R1I1A1A01060310) funded by the Korean government (MSIT).

Based on observations collected at the European Southern Observatory under ESO program ID 179.A-2005 and on data products produced by CALET and the Cambridge Astronomy Survey Unit on behalf of the UltraVISTA consortium.

The `IllustrisTNG` simulations were undertaken with compute time awarded by the Gauss Centre for Supercomputing (GCS) under GCS Large-Scale Projects GCS-ILLU and GCS-DWAR on the GCS share of the supercomputer Hazel Hen at the High Performance Computing Center Stuttgart (textbfRS), as well as on the machines of the Max Planck Computing and Data Facility (MPCDF) in Garching, Germany.

Appendix
Mock Simulation with `TNG300`

We provide a detailed description of how we conducted our analysis of the `TNG300` simulation to interpret the results obtained from COSMOS2020. The `TNG300` simulation identifies galaxy groups with a standard FoF algorithm run on all kinds of particles (dark matter, gas, stars, black holes) as described in D. Nelson et al. (2018). The star formation in `TNG300` is implemented by following the procedure of V. Springel & L. Hernquist (2003). Nevertheless, the star formation rate derived in this manner is instantaneous and not compatible with the star formation rate measured in observations. In order to reflect the observational star formation tracer, we adopt a time-averaged SFR within appropriate apertures. This adjustment is designed to align the simulation's SFR with the observational star formation tracers. Instead of using the SFR given in the group catalog directly, we utilize quantities related to the SFR from M. Donnari et al. (2019) and A. Pillepich et al. (2019). The SFRs in the COSMOS2020 catalog are derived by the SED fitting method, including IR emission and it reflects the SFR in the past ∼100 Myr. Therefore, we employ the time-averaged SFR measured over a timescale of the past 100 Myr. To represent the galaxy-wide star formation activities, the aperture size of twice the stellar half-mass radius is used to calculate the SFR. This derived star formation is not completely comparable to this observational study; however, it is known to affect the QF little because different aperture sizes do not significantly impact the classification between quiescent and star-forming galaxies (see M. Donnari et al. 2019 for further details).

For galaxy clusters, we used the groups with halo masses M_{200} (`Group_M_Crit200`) more massive than $10^{13}\,M_{\odot}$ at each snapshot. Groups located within $10h^{-1}$ Mpc from the edges of the simulation box are excluded from our analysis. To construct a density field comparable to the observational data, three-dimensional grid spacing $200h^{-1}$ kpc is adopted and convolved by a uniform filter of $8 \times 8 \times 8$. We note that the number density field derived from COSMOS2020 has a size of $100\,\mathrm{kpc} \times 100\,\mathrm{kpc} \times 0.01(1+z)$ where the redshift uncertainty of $\sim 0.01(1+z)$ corresponds to a few tens of Mpc. In this regard, our choice of grid spaces and convolution scales is designed to contain a similar number of galaxies in each grid cell in the `TNG300` simulation. The main difference in the FoF fraction between COSMOS2020 and `IllustrisTNG` is that the FoF fraction is a three-dimensional cube in place of a two-dimensional cylindrical volume. We found that the uncertainties derived from the projection effect and photometric redshift do not change the results from the `TNG300` simulation when projecting the density field, as discussed in Section 3.4.

ORCID iDs

Eunhee Ko (고은희) https:/orcid.org/0000-0002-8130-8044
Myungshin Im https://orcid.org/0000-0002-8537-6714
Seong-Kook Lee https://orcid.org/0000-0001-5342-8906

References

Aihara, H., AlSayyad, Y., Ando, M., et al. 2019, PASJ, 71, 114
Alberts, S., & Noble, A. 2022, Univ, 8, 554
Almaini, O., Foucaud, S., Lane, K., et al. 2007, in ASP Conf. Series, Vol. 379, Cosmic Frontiers, ed. N. Metcalfe & T. Shanks (San Francisco, CA: ASP), 163
Alpaslan, M., Grootes, M., Marcum, P. M., et al. 2016, MNRAS, 457, 2287
Alpaslan, M., Robotham, A. S. G., Driver, S., et al. 2014, MNRAS, 438, 177
Anbajagane, D., Evrard, A. E., & Farahi, A. 2022, MNRAS, 509, 3441
Aragon Calvo, M. A., Neyrinck, M. C., & Silk, J. 2019, OJAp, 2, 7
Aragon-Salamanca, A., Ellis, R. S., Couch, W. J., & Carter, D. 1993, MNRAS, 262, 764
Arnouts, S., Moscardini, L., Vanzella, E., et al. 2002, MNRAS, 329, 355
Ashby, M. L. N., Caputi, K. I., Cowley, W., et al. 2018, ApJS, 237, 39
Bai, L., Marcillac, D., Rieke, G. H., et al. 2007, ApJ, 664, 181
Bai, L., Rieke, G. H., Rieke, M. J., Christlein, D., & Zabludoff, A. I. 2009, ApJ, 693, 1840
Baldry, I. K., Balogh, M. L., Bower, R. G., et al. 2006, MNRAS, 373, 469
Baldry, I. K., Glazebrook, K., Brinkmann, J., et al. 2004, ApJ, 600, 681
Balogh, M. L., McGee, S. L., Mok, A., et al. 2016, MNRAS, 456, 4364
Bell, E. F., Wolf, C., Meisenheimer, K., et al. 2004, ApJ, 608, 752
Benjamin, J., Van Waerbeke, L., Ménard, B., & Kilbinger, M. 2010, MNRAS, 408, 1168
Bertin, E., & Arnouts, S. 1996, A&AS, 117, 393
Bialas, D., Lisker, T., Olczak, C., Spurzem, R., & Kotulla, R. 2015, A&A, 576, A103
Bordoloi, R., Lilly, S. J., & Amara, A. 2010, MNRAS, 406, 881
Boselli, A., Roehlly, Y., Fossati, M., et al. 2016, A&A, 596, A11
Bower, R. G., Benson, A. J., Malbon, R., et al. 2006, MNRAS, 370, 645
Brammer, G. B., van Dokkum, P. G., & Coppi, P. 2008, ApJ, 686, 1503
Bremer, M. N., Phillipps, S., Kelvin, L. S., et al. 2018, MNRAS, 476, 12
Brinchmann, J., Charlot, S., White, S. D. M., et al. 2004, MNRAS, 351, 1151
Brodwin, M., Stanford, S. A., Gonzalez, A. H., et al. 2013, ApJ, 779, 138
Brunner, R. J., & Lubin, L. M. 2000, AJ, 120, 2851
Butcher, H., & Oemler, A. J. 1978, ApJ, 219, 18
Catinella, B., Schiminovich, D., Cortese, L., et al. 2013, MNRAS, 436, 34
Catinella, B., Schiminovich, D., Kauffmann, G., et al. 2010, MNRAS, 403, 683
Cautun, M., van de Weygaert, R., & Jones, B. J. T. 2013, MNRAS, 429, 1286
Chiang, Y.-K., Overzier, R., & Gebhardt, K. 2013, ApJ, 779, 127
Chung, S. M., Gonzalez, A. H., Clowe, D., Markevitch, M., & Zaritsky, D. 2010, ApJ, 725, 1536
Cicone, C., Maiolino, R., Sturm, E., et al. 2014, A&A, 562, A21
Codis, S., Pogosyan, D., & Pichon, C. 2018, MNRAS, 479, 973
Cole, S., Lacey, C. G., Baugh, C. M., & Frenk, C. S. 2000, MNRAS, 319, 168
Cooper, M. C., Newman, J. A., Madgwick, D. S., et al. 2005, ApJ, 634, 833
Coupon, J., Czakon, N., Bosch, J., et al. 2018, PASJ, 70, S7
Crone Odekon, M., Hallenbeck, G., Haynes, M. P., et al. 2018, ApJ, 852, 142
Croton, D. J., Springel, V., White, S. D. M., et al. 2006, MNRAS, 365, 11
Cui, W., Knebe, A., Yepes, G., et al. 2018, MNRAS, 480, 2898
Dalla Vecchia, C., & Schaye, J. 2008, MNRAS, 387, 1431
Damen, M., Labbé, I., Franx, M., et al. 2009, ApJ, 690, 937
Darragh Ford, E., Laigle, C., Gozaliasl, G., et al. 2019, MNRAS, 489, 5695
Darvish, B., Mobasher, B., Martin, D. C., et al. 2017, ApJ, 837, 16
Darvish, B., Mobasher, B., Sobral, D., et al. 2016, ApJ, 825, 113
Darvish, B., Sobral, D., Mobasher, B., et al. 2014, ApJ, 796, 51
Davidzon, I., Ilbert, O., Laigle, C., et al. 2017, A&A, 605, A70
Davis, M., Efstathiou, G., Frenk, C. S., & White, S. D. M. 1985, ApJ, 292, 371
De Lucia, G., Poggianti, B. M., Aragón-Salamanca, A., et al. 2007, MNRAS, 374, 809
Dekel, A., & Silk, J. 1986, ApJ, 303, 39
Di Matteo, P., Combes, F., Melchior, A. L., & Semelin, B. 2007, A&A, 468, 61
Di Matteo, T., Springel, V., & Hernquist, L. 2005, Natur, 433, 604
Dolag, K., Borgani, S., Murante, G., & Springel, V. 2009, MNRAS, 399, 497
Donnari, M., Pillepich, A., Joshi, G. D., et al. 2021a, MNRAS, 500, 4004
Donnari, M., Pillepich, A., Nelson, D., et al. 2019, MNRAS, 485, 4817
Donnari, M., Pillepich, A., Nelson, D., et al. 2021b, MNRAS, 506, 4760
Dubois, Y., Peirani, S., Pichon, C., et al. 2016, MNRAS, 463, 3948
Dubois, Y., Pichon, C., Welker, C., et al. 2014, MNRAS, 444, 1453
Einasto, M., Deshev, B., Tenjes, P., et al. 2020, A&A, 641, A172
Fabian, A. C. 2012, ARA&A, 50, 455
Fadda, D., Biviano, A., Marleau, F. R., Storrie-Lombardi, L. J., & Durret, F. 2008, ApJL, 672, L9
Fang, J. J., Faber, S. M., Koo, D. C., & Dekel, A. 2013, ApJ, 776, 63
Fang, Y., Clampitt, J., Dalal, N., et al. 2016, MNRAS, 463, 1907
Foltz, R., Wilson, G., Muzzin, A., et al. 2018, ApJ, 866, 136
Gal, R. R., de Carvalho, R. R., Odewahn, S. C., Djorgovski, S. G., & Margoniner, V. E. 2000, AJ, 119, 12
Galárraga-Espinosa, D., Garaldi, E., & Kauffmann, G. 2023, A&A, 671, A160
Geach, J. E., Smail, I., Moran, S. M., et al. 2011, ApJL, 730, L19
Gouin, C., Bonnaire, T., & Aghanim, N. 2021, A&A, 651, A56
Gozaliasl, G., Finoguenov, A., Tanaka, M., et al. 2019, MNRAS, 483, 3545
Gunn, J. E., & Gott, J. R. I. 1972, ApJ, 176, 1
Haggar, R., Kuchner, U., Gray, M. E., et al. 2023, MNRAS, 518, 1316
Haines, C. P., Pereira, M. J., Smith, G. P., et al. 2015, ApJ, 806, 101
Hashimoto, Y., Oemler, Augustus, J., Lin, H., & Tucker, D. L. 1998, ApJ, 499, 589
Hatfield, P. W., & Jarvis, M. J. 2017, MNRAS, 472, 3570
Hoaglin, D. C., Mosteller, F., & Tukey, J. W. 1983, Understanding robust and exploratory data anlysis (New York: Wiley)
Hogg, D. W., Blanton, M. R., Brinchmann, J., et al. 2004, ApJL, 601, L29

Hung, C.-L., Casey, C. M., Chiang, Y.-K., et al. 2016, ApJ, 826, 130
Ilbert, O., Arnouts, S., Le Floc'h, E., et al. 2015, A&A, 579, A2
Ilbert, O., Arnouts, S., McCracken, H. J., et al. 2006, A&A, 457, 841
Ilbert, O., McCracken, H. J., Le Fèvre, O., et al. 2013, A&A, 556, A55
Janowiecki, S., Catinella, B., Cortese, L., et al. 2017, MNRAS, 466, 4795
Jian, H.-Y., Lin, L., Lin, K.-Y., et al. 2017, ApJ, 845, 74
Kang, E., & Im, M. 2009, ApJL, 691, L33
Kang, E., & Im, M. 2015, JKAS, 48, 21
Kawinwanichakij, L., Papovich, C., Quadri, R. F., et al. 2017, ApJ, 847, 134
Kleiner, D., Pimbblet, K. A., Jones, D. H., Koribalski, B. S., & Serra, P. 2017, MNRAS, 466, 4692
Klypin, A., Yepes, G., Gottlöber, S., Prada, F., & Heß, S. 2016, MNRAS, 457, 4340
Kotecha, S., Welker, C., Zhou, Z., et al. 2022, MNRAS, 512, 926
Kovač, K., Lilly, S. J., Knobel, C., et al. 2014, MNRAS, 438, 717
Koyama, Y., Kodama, T., Shimasaku, K., et al. 2008, MNRAS, 391, 1758
Kraljic, K., Pichon, C., Codis, S., et al. 2020, MNRAS, 491, 4294
Kraljic, K., Pichon, C., Dubois, Y., et al. 2019, MNRAS, 483, 3227
Kuchner, U., Haggar, R., Aragón-Salamanca, A., et al. 2022, MNRAS, 510, 581
Labbé, I., Huang, J., Franx, M., et al. 2005, ApJL, 624, L81
Laigle, C., Davidzon, I., Ilbert, O., et al. 2019, MNRAS, 486, 5104
Laigle, C., McCracken, H. J., Ilbert, O., et al. 2016, ApJS, 224, 24
Laigle, C., Pichon, C., Arnouts, S., et al. 2018, MNRAS, 474, 5437
Laigle, C., Pichon, C., Codis, S., et al. 2015, MNRAS, 446, 2744
Lang, D., Hogg, D. W., & Mykytyn, D., 2016 The Tractor: Probabilistic Astronomical Source Detection and Measurement, Astrophysics Source Code Library, record, ascl:1604.008
Larson, R. B. 1974, MNRAS, 166, 585
Larson, R. B., Tinsley, B. M., & Caldwell, C. N. 1980, ApJ, 237, 692
Leauthaud, A., Finoguenov, A., Kneib, J.-P., et al. 2010, ApJ, 709, 97
Lee, S.-K., Im, M., Hyun, M., et al. 2019, MNRAS, 490, 135
Lee, S.-K., Im, M., Kim, J.-W., et al. 2015, ApJ, 810, 90
Le Fèvre, O., Tasca, L. A. M., Cassata, P., et al. 2015, A&A, 576, A79
Lemaux, B. C., Gal, R. R., Lubin, L. M., et al. 2012, ApJ, 745, 106
Libeskind, N. I., van de Weygaert, R., Cautun, M., et al. 2018, MNRAS, 473, 1195
Lilly, S. J., Le Fèvre, O., Renzini, A., et al. 2007, ApJS, 172, 70
Lin, L., Jian, H.-Y., Foucaud, S., et al. 2014, ApJ, 782, 33
Łokas, E. L. 2020, A&A, 638, A133
Lovisari, L., Ettori, S., Gaspari, M., & Giles, P. A. 2021, Univ, 7, 139
Lu, S., Xu, D., Wang, S., et al. 2022, MNRAS, 509, 2707
Lubin, L. M., Gal, R. R., Lemaux, B. C., Kocevski, D. D., & Squires, G. K. 2009, AJ, 137, 4867
Mahajan, S., Raychaudhury, S., & Pimbblet, K. A. 2012, MNRAS, 427, 1252
Malavasi, N., Pozzetti, L., Cucciati, O., Bardelli, S., & Cimatti, A. 2016, A&A, 585, A116
Martin, G., Kaviraj, S., Devriendt, J. E. G., et al. 2017, MNRAS, 472, L50
McCracken, H. J., Milvang-Jensen, B., Dunlop, J., et al. 2012, A&A, 544, A156
McCracken, H. J., Wolk, M., Colombi, S., et al. 2015, MNRAS, 449, 901
McGee, S. L., Balogh, M. L., Bower, R. G., Font, A. S., & McCarthy, I. G. 2009, MNRAS, 400, 937
McGee, S. L., Bower, R. G., & Balogh, M. L. 2014, MNRAS, 442, L105
Merson, A. I., Baugh, C. M., Helly, J. C., et al. 2013, MNRAS, 429, 556
Moneti, A., McCracken, H. J., Hudelot, W., et al. 2023, VizieR Online Data Catalog, 2373. II/373
Moore, B., Katz, N., Lake, G., Dressler, A., & Oemler, A. 1996, Natur, 379, 613
More, S., Kravtsov, A. V., Dalal, N., & Gottlöber, S. 2011, ApJS, 195, 4
Moster, B. P., Somerville, R. S., Newman, J. A., & Rix, H.-W. 2011, ApJ, 731, 113
Muldrew, S. I., Hatch, N. A., & Cooke, E. A. 2015, MNRAS, 452, 2528
Musso, M., Cadiou, C., Pichon, C., et al. 2018, MNRAS, 476, 4877
Muzzin, A., Wilson, G., Yee, H. K. C., et al. 2012, ApJ, 746, 188
Navarro, J. F., Frenk, C. S., & White, S. D. M. 1997, ApJ, 490, 493
Nayyeri, H., Hemmati, S., Mobasher, B., et al. 2017, ApJS, 228, 7
Nelson, D., Pillepich, A., Springel, V., et al. 2018, MNRAS, 475, 624
Newman, J. A., & Gruen, D. 2022, ARA&A, 60, 363
Oh, S., Mulchaey, J. S., Woo, J.-H., et al. 2014, ApJ, 790, 43
Oke, J. B. 1974, ApJS, 27, 21
O'Sullivan, E., Ponman, T. J., Kolokythas, K., et al. 2017, MNRAS, 472, 1482
Peng, Y.-j., Lilly, S. J., Kovač, K., et al. 2010, ApJ, 721, 193
Pillepich, A., Nelson, D., Springel, V., et al. 2019, MNRAS, 490, 3196
Pillepich, A., Springel, V., Nelson, D., et al. 2018, MNRAS, 473, 4077
Pintos-Castro, I., Yee, H. K. C., Muzzin, A., Old, L., & Wilson, G. 2019, ApJ, 876, 40
Porter, S. C., & Raychaudhury, S. 2007, MNRAS, 375, 1409
Pozzetti, L., Bolzonella, M., Zucca, E., et al. 2010, A&A, 523, A13
Rost, A., Kuchner, U., Welker, C., et al. 2021, MNRAS, 502, 714
Rost, A. M., Nuza, S. E., Stasyszyn, F., et al. 2024, MNRAS, 527, 1301
Sarron, F., Martinet, N., Durret, F., & Adami, C. 2018, A&A, 613, A67
Schiminovich, D., Wyder, T. K., Martin, D. C., et al. 2007, ApJS, 173, 315
Scoville, N., Arnouts, S., Aussel, H., et al. 2013, ApJS, 206, 3
Scoville, N., Aussel, H., Brusa, M., et al. 2007, ApJS, 172, 1
Sengupta, A., Keel, W. C., Morrison, G., et al. 2022, ApJS, 258, 32
Seppi, R., Comparat, J., Bulbul, E., et al. 2022, A&A, 665, A78
Shattow, G. M., Croton, D. J., Skibba, R. A., et al. 2013, MNRAS, 433, 3314
Shen, Y., Mulchaey, J. S., Raychaudhury, S., Rasmussen, J., & Ponman, T. J. 2007, ApJL, 654, L115
Smethurst, R. J., Lintott, C. J., Simmons, B. D., et al. 2015, MNRAS, 450, 435
Smith, R., Davies, J. I., & Nelson, A. H. 2010, MNRAS, 405, 1723
Song, H., Laigle, C., Hwang, H. S., et al. 2021, MNRAS, 501, 4635
Sousbie, T. 2011, MNRAS, 414, 350
Speagle, J. S., Steinhardt, C. L., Capak, P. L., & Silverman, J. D. 2014, ApJS, 214, 15
Springel, V. 2005, MNRAS, 364, 1105
Springel, V., & Hernquist, L. 2003, MNRAS, 339, 289
Springel, V., Pakmor, R., Pillepich, A., et al. 2018, MNRAS, 475, 676
Springel, V., White, S. D. M., Tormen, G., & Kauffmann, G. 2001, MNRAS, 328, 726
Stott, J. P. 2007, PhD thesis, Durham Univ.
Strateva, I., Ivezić, Ž., Knapp, G. R., et al. 2001, AJ, 122, 1861
Tanaka, M., Kodama, T., Arimoto, N., et al. 2005, MNRAS, 362, 268
Tanaka, M., Lidman, C., Bower, R. G., et al. 2009, A&A, 507, 671
Taniguchi, Y., Kajisawa, M., Kobayashi, M. A. R., et al. 2015, PASJ, 67, 104
Taniguchi, Y., Scoville, N., Murayama, T., et al. 2007, ApJS, 172, 9
Taranu, D. S., Hudson, M. J., Balogh, M. L., et al. 2014, MNRAS, 440, 1934
Tempel, E., Stoica, R. S., Martínez, V. J., et al. 2014, MNRAS, 438, 3465
van der Burg, R. F. J., McGee, S., Aussel, H., et al. 2018, A&A, 618, A140
Vurm, I., Nevalainen, J., Hong, S. E., et al. 2023, A&A, 673, A62
Weaver, J. R., Davidzon, I., Toft, S., et al. 2023, A&A, 677, A184
Weaver, J. R., Kauffmann, O. B., Ilbert, O., et al. 2022, ApJS, 258, 11
Werner, S. V., Hatch, N. A., Muzzin, A., et al. 2022, MNRAS, 510, 674
Wetzel, A. R., Tinker, J. L., & Conroy, C. 2012, MNRAS, 424, 232
Wetzel, A. R., Tinker, J. L., Conroy, C., & van den Bosch, F. C. 2013, MNRAS, 432, 336
Whitaker, K. E., van Dokkum, P. G., Brammer, G., & Franx, M. 2012, ApJL, 754, L29
Williams, R. J., Quadri, R. F., Franx, M., van Dokkum, P., & Labbé, I. 2009, ApJ, 691, 1879
Winkel, N., Pasquali, A., Kraljic, K., et al. 2021, MNRAS, 505, 4920
Wuyts, S., Labbé, I., Franx, M., et al. 2007, ApJ, 655, 51